

A search for clusters at high redshift

III. Candidate H α emitters and EROs in the PKS 1138–262 proto-cluster at $z = 2.16$

J. D. Kurk¹, L. Pentericci², H. J. A. Röttgering¹, and G. K. Miley¹

¹ Sterrewacht Leiden, P.O. Box 9513, 2300 RA, Leiden, The Netherlands

² Max-Planck-Institut für Astronomie, Königstuhl 17, D-69117, Heidelberg, Germany

Received date / Accepted date

Abstract. In this paper we present deep VLT multi wavelength imaging observations of the field around the radio galaxy PKS 1138–262 aimed at detecting and studying a (potential) proto-cluster centered at this radio source. PKS 1138–262 is a massive galaxy at $z = 2.16$, located in a dense environment as indicated by optical, X-ray and radio observations. We had already found an over-density of Ly α emitting galaxies in this field, consistent with a proto-cluster structure associated with the radio galaxy. In addition, we find 40 candidate H α emitters that have nominal rest frame equivalent width $> 25 \text{ \AA}$ within 1.8 Mpc and 2000 km s^{-1} of the radio galaxy. Furthermore, we find 44 objects with $I - K > 4.3$. This number of extremely red objects (EROs) is about twice the number found in blank field ERO surveys, suggesting that some EROs in this field are part of the proto-cluster. The density of H α emitters and extremely red objects increases towards the radio galaxy, indicating a physical association. From comparisons with other K band, ERO, H α and Ly α surveys, we conclude that PKS 1138–262 is located in a density peak which will evolve into a cluster of galaxies.

Key words. Galaxies: active – Galaxies: clusters: general – Galaxies: evolution – Galaxies: luminosity function – Cosmology: observations – Cosmology: early Universe

1. Introduction

The search for clusters at high redshift has two main incentives: distant clusters can be used to constrain cosmological models and they provide a reservoir of high redshift galaxies, which can be used to study galaxy formation and evolution.

According to hierarchical clustering theories, clusters form by the gravitational amplification of primordial density fluctuations. In a low density universe, fluctuations cease to grow after a redshift $z \sim (\Omega_0^{-1} - 1)$ (Peebles 1980), resulting in a cluster population that evolves very slowly at low redshift. In an $\Omega_0 = 1$ universe density fluctuations continue to grow even at the present epoch, implying that the cluster population would still be evolving rapidly (Eke et al. 1996). The detection of even a single distant massive cluster, such as MS 1054–03 at $z = 0.83$, constrains the parameters (Ω_0, σ_8) of cosmological models (Bahcall & Fan 1998; Donahue et al. 1998).

The study of galaxies in nearby and distant clusters provides strong constraints on their evolution and formation. It has been shown that clusters at high redshift

can contain a different galaxy population mix than those at low redshift. Butcher & Oemler (1984) found that at $0.1 < z < 0.5$, compact clusters have significant numbers of blue galaxies, the fraction increasing with redshift, while at $z < 0.1$ cluster cores are essentially devoid of these. This effect can be explained if we assume a process in which spirals lose their gas and ability to form stars or are converted into early type galaxies in the course of their evolution. Massive ellipticals, however, dominating cluster cores up to $z \sim 1$ seem to form a homogeneous population. Even at $z = 1.27$, van Dokkum et al. (2001) observe a scatter of the colour-magnitude relation of cluster galaxies similar to that in lower redshift clusters.

The tight colour-magnitude relation observed out to high redshifts can be explained by several galaxy formation scenarios. De Propris et al. (1999) propose a passive luminosity evolution model, where galaxies form all their stars in a single burst at $z = 2$ after a monolithic collapse (e.g. Eggen et al. 1962). van Dokkum & Franz (2001) show that the observations are also consistent with a scenario in which early-type galaxies are continuously transformed from spiral galaxies, causing the progenitors of the youngest, low redshift early-type galaxies to drop out of the sample at higher redshifts (*progeni-*

tor bias). Models by van Dokkum & Franx (2001) show that about half of the early-type galaxies were morphologically transformed at $z < 1$ and their progenitors may have had roughly constant star formation rates before transformation. These models indicate a mean luminosity weighted formation of stars in early-type galaxies of $z = 2.0$ (for $\Omega_M = 0.3$ and $\Omega_\Lambda = 0.7$), consistent with the currently favoured hierarchical galaxy formation models predicting the merging of smaller galaxies at high redshift (Kauffmann 1996). A third explanation is given by metallicity differences in bright and faint ellipticals. A model by Kauffmann & Charlot (1998) which includes hierarchical formation of ellipticals out of disc galaxies which have formed stars at modest rates and allows for the ejection of metals out of discs by supernova explosions predicts the establishment of a mass-metallicity relation among both late- and early-type galaxies. In this model, large ellipticals are more metal-rich because they are formed from the mergers of larger discs.

The strongest observational constraints on these models come from the highest redshift data. Both for the study of cluster and galaxy evolution a sample of clusters at high redshift is therefore desired.

In recent years, much effort has been invested in the search for distant clusters, using both optical and X-ray observations. At $z > 0.5$, it becomes difficult to identify the projected two-dimensional over-density produced by cluster galaxies, because large numbers of foreground and background galaxies reduce the density contrast in the optical wavelength regime. However, the $J - K$ colour of nearly all galaxies out to $z = 2$ is a simple function of redshift, because their near infrared light is dominated by evolved giant stars. The highest redshift cluster found to date (Stanford et al. 1997, CIG J0848+4453 at $z = 1.27$) has been discovered in a near infrared field survey as a high density region of objects with very red $J - K$ colours. Optical spectroscopy confirmed the redshifts of eight members and a 4.5σ ROSAT X-ray detection confirms the cluster's existence. Although the detectability of hot cluster gas in X-rays is severely reduced by cosmological surface brightness dimming, Rosati et al. (1998) has found within the ROSAT Deep Cluster Survey a cluster at $z = 1.11$ (Stanford et al. 2002, RDCS J0910+5422) with 9 spectroscopically confirmed cluster members and a cluster at $z = 1.26$ (Rosati et al. 1999, RX J0848.9+4452) with 6 cluster members confirmed. Most of the confirmed galaxies have red colours, consistent with passively evolved ellipticals formed at high redshift ($z \sim 5$). The latter cluster is very close to CIG J0848+4453, with which it might form a superstructure and is possibly in the process of merging. The recently started XMM Large Scale Structure Survey (Refregier et al. 2002), covering over 64 square degrees of sky, should be able to detect clusters with X-ray luminosities of 2×10^{44} erg s $^{-1}$ out to $z = 2$. Despite the success of the near infrared and X-ray techniques, it is difficult to push these methods to find $z \gg 1$ over-densities.

A practical way to find clusters and groups of galaxies at high redshift is to study fields containing luminous radio galaxies. These can be observed up to the epoch of galaxy formation and efficiently selected by their steep spectrum in the radio regime (Röttgering et al. 1994; Lacy et al. 1994; De Breuck et al. 2000). The most distant radio galaxy found to date has a redshift of 5.2 (van Breugel et al. 1999). The host galaxies of powerful radio sources are amongst the most massive at any redshift (Jarvis et al. 2001; De Breuck et al. 2002) and are associated with $\sim 10^9 M_\odot$ BHs (Lacy et al. 2001; McLure & Dunlop 2002).

There has long been evidence that powerful radio galaxies at high redshift (HzRGs, $z > 2$) are located in the center of (forming) clusters of galaxies. Yates et al. (1989) and Hill & Lilly (1991) find that the average environment of 70 powerful classical double radio sources at $0.15 < z < 0.82$ is that of an Abell 0 cluster, with some in environments as rich as Abell class 1. At $z \sim 1$ and higher, there is also evidence for galaxy over-densities associated with radio galaxies. Best (2000) presents an analysis of the environments of 28 3CR radio galaxies at $0.6 < z < 1.8$. The density of K -band galaxies in these field, their angular cross correlation amplitude and near infrared colours correspond to the properties of low redshift Abell richness class 0 to 1 clusters. The author concludes that many, but not all, powerful radio galaxies at $z \sim 1$ lie in cluster environments. Furthermore, Nakata et al. (2001) have applied a photometric redshift technique based on five optical and near infrared images of the field of 3C324 at $z = 1.2$ and identified 35 objects as plausible cluster members. The evidence extends even to $z = 3.8$, where observations in the field of radio galaxy 4C41.17 by Ivison et al. (2000) tentatively reveal a number of luminous submm galaxies over-dense by an order of magnitude as compared to typical fields.

There is also evidence that the environments of HzRGs are dense in terms of ambient gas, as expected for the centers of (forming) clusters. Radio continuum observations of ~ 70 radio galaxies at $z \sim 2$ (Carilli et al. 1997; Pentericci et al. 2000b) show that 20 – 30% have large (≥ 1000 rad m $^{-2}$) radio rotation measures (RMs). These RMs are most probably due to magnetized, ionized gas local to the radio sources and are comparable to the RMs of lower redshift radio galaxies which lie in the centers of dense, X-ray emitting cluster atmospheres (Taylor et al. 1994).

Although convincing evidence for high density environments associated with radio galaxies at $z > 1$ has been demonstrated, the redshifts of possible cluster members have not been confirmed by spectroscopy and it is therefore impossible to provide a velocity dispersion for these structures. In a program which is currently being carried out with the VLT, we are targeting the fields of luminous radio galaxies at $z > 2$ and observe these with the aim of detecting line emitting galaxies in the associated cluster. At $z > 2$ the Ly α line is redshifted into the optical wave-

length region, where we can use narrow band filters ($\sim 1\%$) to isolate its flux from the sky background. We have selected ten luminous radio galaxies at $2.2 < z < 5.2$, for which we will carry out both imaging and multi object spectroscopy. The survey is progressing very well and has already produced the discovery of the most distant structure of galaxies known (at $z = 4.1$, Venemans et al. 2002).

We consider the Ly α imaging and spectroscopy as a first step to the characterization of the cluster properties. The Ly α emitters in a cluster form only a fraction of the galaxies present and might not be representative for some of the cluster or galaxy properties. The program will therefore be followed up by e.g. broad band imaging in several colours. In this paper, we present new optical and near infrared observations of the field of PKS 1138–262 with the aim of uncovering populations of H α emitting galaxies and EROs in the structure.

The radio galaxy PKS 1138–262 at a redshift of 2.16, was selected from a compendium of more than 150 $z > 2$ radio galaxies as the optimum object for beginning a high redshift cluster search. It combines most of the above mentioned cluster indications with a redshift suitable for both Ly α and H α imaging. The magnitude of 1138–262 is the brightest of all known radio galaxies close to $z = 2$. After correction for possible non stellar components, the K band magnitude is 16.8, from which a stellar mass of $10^{12} M_\odot$ was inferred (Pentericci et al. 1997). The radio galaxy possesses a giant (~ 120 kpc) and luminous Ly α nebula, with a wealth of structure: a bright region associated with the radio jet and filaments extending over > 40 kpc (Pentericci et al. 1997; Kurk et al. 2000b). The optical counterpart of the radio galaxy is extremely clumpy and resolved into many components by the HST (Pentericci et al. 1998). These clumps have properties similar to LBGs. The morphology of the system is consistent with hierarchical models of galaxy formation in which the LBG building blocks will merge into a single massive system, such as the massive galaxies observed at the centers of some rich clusters. The extremely distorted radio morphology (Carilli et al. 1997) is strong evidence that the jets have been deflected from their original direction by a dense and clumpy medium. The observed rotation measures of the radio emission (6200 rad m^{-1} , the largest in a sample of 70 HzRGs, see Carilli et al. 1997; Pentericci et al. 2000b) and its steep gradient over the radio galaxy components also testify that the radio source is embedded in a dense magnetized medium. Additional evidence for a dense surrounding medium comes from *Chandra* X-ray observations, which reveal thermal emission from shocked gas (Carilli et al. 2002). The pressure of this hot gas is adequate to confine the radio source.

Narrow band imaging of redshifted Ly α emission of a $7' \times 7'$ region around the radio galaxy (Kurk et al. 2000a, Paper I) and subsequent Ly α spectroscopy (Pentericci et al. 2000a, Paper II) revealed 14 Ly α emitting galaxies and one QSO. The galaxies have redshifts in the range 2.16 ± 0.02 with a velocity dispersion substan-

tially smaller than expected for a random sample of galaxies selected by the narrow band filter. In addition, the *Chandra* X-ray observations of the field of 1138–262 have revealed at least five AGN at $z \sim 2.16$ (Pentericci et al. 2002). On the basis of the evidence from the radio galaxy properties, the Ly α halo and the galaxy over-density, we concluded that the structure of galaxies surrounding PKS 1138–262 is (the progenitor of) a cluster.

The new observations of 1138–262 are reported in Sect. 2. Detection and photometry of objects in the field of 1138–262 are presented in Sect. 3. Subsequently, the selection from these objects of K band galaxies, EROs, candidate H α emitters and candidate Ly α emitters is presented in Sect. 4. The properties of the EROs and candidates are analyzed in Sect. 5. A discussion of the implications of these results for the nature of the structure can be found in Sect. 6, which is followed by a summary of the results and conclusions in Sect. 7. Throughout this article, we adopt a Hubble constant of $H_0 = 65 \text{ km s}^{-1} \text{Mpc}^{-1}$ and a Λ dominated cosmology: $\Omega_M = 0.3$ and $\Omega_\Lambda = 0.7$. The over-densities of galaxies at high redshift, which have not yet reached virialization and/or a colour-magnitude relation with a red sequence, but will later form clusters, will be called *proto-clusters* here.

2. Observations and data reduction

2.1. Optical observations

The observations of PKS 1138–262 were carried out with the VLT¹. With the aim of detecting Ly α emitting galaxies at $z = 2.16$, we have observed the field of 1138–262 for half an hour in B band and four hours in a 2% narrow band, using FORS1 at Antu (UT1). Subsequent multi object spectroscopy of candidate emitters was also carried out with FORS1, employing three masks with integration times of 4 to 6 hours. The optical imaging and spectroscopy observations are described in detail in Paper I and II. For an overview of both old and new observations, see Table 1.

We have complemented the original optical imaging with broad band observations in R and I , using FORS2 at Kueyen (UT2) in 2001. The detector of FORS2 was a Tektronix thinned and anti-reflection coated CCD with 2048×2048 pixels and a scale of $0''.2$ per pixel in standard resolution mode, yielding a field size of $\sim 6''.8 \times 6''.8$. Six exposures of 5 minutes during non-photometric conditions were taken through the R _Special filter, which has a central wavelength of 6550 \AA and FWHM of 1650 \AA . The R _Special filter has higher transmission than the standard Bessel R filter and its transmission curve is almost symmetrical around the central wavelength, while the Bessel filter has its peak at 6000 \AA and declines towards the red. Six non-photometric exposures of 7.5 minutes were

¹ Based on observations carried out at the European Southern Observatory, Paranal, Chile, programmes P63.O-0477(A&D), P65.O-0324(B), and P66.A-0597(B&D).

taken in service mode through the Bessel *I* filter, which has a central wavelength of 7680 Å and FWHM of 1380 Å. During visitor time, three weeks later, an additional eighteen photometric exposures of 5 minutes were observed. The observations were made employing a jittering pattern with offsets $< 20''$ between exposures to minimize flat fielding problems and to facilitate cosmic ray removal. The seeing on the resultant images and the 3σ limiting magnitude in a $1''$ aperture as measured on the central square arcminute of the combined images is listed in Table 2.

Image reduction was carried out using the IRAF² reduction package. The individual frames were bias subtracted, flat fielded with twilight flats and cosmic rays were removed. The frames were combined using the DIMSUM³ package. DIMSUM builds a cumulative sky frame from 6 to 10 subsequent unregistered images. Objects in the unregistered frames were detected with SExtractor (Bertin & Arnouts 1996) and masked during the process of background determination. The obtained sky frames were subtracted from the images. The image offsets were determined by measuring the positions of a number (~ 20) of stars on each frame. Pixels on the CCD which were significantly discrepant in each sky frame were marked as bad pixels and the exposure time for each pixel was computed by DIMSUM. This exposure map is later used as a weight map for object detection and photometry. In the last step of the process, all individual broad band frames were combined by averaging while identified cosmic rays and bad pixels were omitted. The registered narrow band images were combined by computing the average of each pixel stack and rejecting pixels whose intensity levels were 10σ above or below the noise level expected from the CCD gain and readout noise specifications.

For the flux calibration of the photometric data the standard stars GD108 (Oke 1990) and LTT4816 (Hamuy et al. 1992, 1994) were used. The *I* band data obtained during non-photometric conditions was scaled to the photometric *I* band data and the *R* band data was calibrated using an older *R* band image of 1138–262 from Pentericci et al. (1997). Astrometric calibration was carried out by identifying 18 stars in the USNO-A2.0 catalogue (Monet et al. 1998), which is tied to the Tycho catalogue (Hoeg et al. 1997). The absolute astrometric accuracy obtained in this way is $\sim 0''.2$.

Note that the narrow and broad band images obtained in 1999 (Paper I) were reduced again. This time we used DIMSUM and obtained a homogeneously reduced set of images in all observed optical and infrared bands. To overcome differences in geometrical distortion, all images were mapped to match the *R* band image. In this way, we have

² IRAF is distributed by the National Optical Astronomy Observatories, which are operated by the Association of Universities for Research in Astronomy, Inc., under cooperative agreement with the National Science Foundation.

³ DIMSUM is a set of scripts to reduce dithered images contributed to IRAF and written by P. Eisenhardt, M. Dickinson, A. Stanford, J. Ward and F. Valdes.

obtained a first set of images with their original spatial resolution. A second set was made in which the *I*, *B* and narrow band ([O II]/8000, called NB 0.38 from now on) images were convolved with the kernel required to match their point spread functions to the *R* band image, which had the worst seeing conditions during observations. The pixel-to-pixel alignment in the final images is accurate to within a pixel ($0''.2$) over the entire image.

2.2. Infrared observations

In 2000 and 2001 Antu's infrared camera ISAAC was employed to carry out imaging of the field of 1138–262 in several near infrared broad bands and a narrow band that included the redshifted H α emission line (He I filter, NB 2.07 from now on). The short wavelength camera of ISAAC is equipped with a Rockwell Hawaii 1024² pixel Hg:Cd:Te array which has a pixel scale of $0.147''$, yielding a field of $\sim 2''.5 \times 2''.5$. This is significantly smaller than the field covered by the optical observations, so we carried out two pointings in the infrared: one centered at the position of the radio galaxy as the optical observations ($\alpha, \delta_{J2000} = 11^{\text{h}}40^{\text{m}}48^{\text{s}}, -26^{\circ}29'10''$, hereafter $\mathcal{F}1$) and one to the North East ($\alpha, \delta_{J2000} = 11^{\text{h}}40^{\text{m}}57^{\text{s}}, -26^{\circ}28'48''$, hereafter $\mathcal{F}2$) covering six confirmed Ly α emitters (Paper II).

All infrared images were taken in jitter mode, where the telescope is offset randomly between exposures but never farther from the original pointing than $20''$. In *J_s*, *H* and *K_s* individual frames were exposed for 100 to 225 seconds using sub-integrations of length 10 to 45 seconds to avoid over-exposure of the background. The narrow band frames were exposed for 300 or 375 seconds with sub-integrations of 60 to 75 seconds respectively. Specifications (date, mode, band, integration time and pointing) of all observations are presented in Table 1. Note that only $\mathcal{F}1$ was observed in *J_s* and *H* band. Observations in *K_s* of $\mathcal{F}1$ were taken in ESO period 63 (P63, 1999) and period 66 (P66, 2001). The sensitivity in P66 had increased by 45% compared to P63, amongst others due to an aluminization of the main mirror. We have scaled the measurements done in P63 to P66, effectively reducing the formal exposure time in P63. The total exposure time in *K_s* for $\mathcal{F}1$ in terms of P66 time units is 1.6 hours.

The infrared observations were reduced in the same way as the optical ones. However, the atmospheric emission in the near infrared is variable on a time scale comparable with the exposure time of individual frames, causing fringing residuals in the frames after background subtraction using the median of six to ten frames. These residuals had to be removed in the *K_s* and NB 2.07 frames observed in 2000 by subtracting a low order polynomial fit to the lines and columns of the masked images. An overview of total exposure time, limiting magnitude and resultant seeing can be found in Table 2.

The infrared images were registered with the optical reference image using the same pixel scale. In $\mathcal{F}1$ 37 objects were used for the alignment and in $\mathcal{F}2$ 40, resulting

Table 1. Observations and filter properties

Date (1)	M (2)	Tel/Instr (3)	Filter (4)	λ_c (5)	λ_{fwhm} (6)	Exp (7)	Time (8)	P (9)
12-4-1999	V	UT1/FORS1	<i>B</i> Bessel	429	88	300	1800	1
12-4-1999	V	UT1/FORS1	NB 0.38	381.4	6.5	1800	9000	1
13-4-1999	V	UT1/FORS1	NB 0.38	381.4	6.5	1800	5400	1
6-3-2001	S	UT2/FORS2	<i>R</i> Special	655	165	300	1800	1
5-3-2001	S	UT2/FORS2	<i>I</i> Bessel	768	138	450	2700	1
27-3-2001	V	UT2/FORS2	<i>I</i> Bessel	768	138	300	5400	1
6-1-2001	S	UT1/ISAAC	J_s	1240	160	45/5	3600	1
17-4-2000	S	UT1/ISAAC	H	1650	300	13/8	2496	1
3-4-1999	S	UT1/ISAAC	K_s	2160	270	10/10	2900	1
4-4-1999	S	UT1/ISAAC	K_s	2160	270	10/10	1900	1
6-1-2001	S	UT1/ISAAC	K_s	2160	270	13/8	2496	1
16-4-2000	S	UT1/ISAAC	NB 2.07	2070	26	60/5	5700	1
17-4-2000	S	UT1/ISAAC	NB 2.07	2070	26	60/5	6300	1
19-4-2000	S	UT1/ISAAC	NB 2.07	2070	26	60/5	5400	1
10-1-2001	S	UT1/ISAAC	K_s	2160	270	13/8	4576	2
11-1-2001	S	UT1/ISAAC	NB 2.07	2070	26	75/5	9000	2
7-2-2001	S	UT1/ISAAC	NB 2.07	2070	26	75/5	6000	2
21-2-2001	S	UT1/ISAAC	NB 2.07	2070	26	75/5	2250	2

Notes: (1) Date: Day – Month – Year (2) Visitor (V) or Service (S) mode (3) Telescope and instrument (4) ESO filter name (5) Filter central wavelength in nm (6) Filter full width at half maximum in nm (7) Exposure time for single frames in seconds; for IR observations DIT/NDIT where DIT is integration time for sub-integration and NDIT number of sub-integrations (8) Total exposure time in seconds (9) Pointing on $\mathcal{F}1$ or $\mathcal{F}2$ (see Sect. 2.2).

Table 2. Resultant images

Band (1)	T (2)	Size (3)	M_{lim} (4)	Seeing (5)
NB 0.38	4.0	46.6	26.5	0.75''
<i>B</i>	0.5	46.6	27.5	0.70''
<i>R</i>	0.5	46.6	26.4	0.85''
<i>I</i>	2.0	46.6	26.8	0.65''
J_s	1.0	7.5	24.8	0.45''
H	0.7	7.5	23.8	0.70''
K_s	1.6	12.5	23.0	0.45''
NB 2.07	4.8	12.5	22.8	0.50''

Notes: (1) Broad band or narrow band (see Table 1 for specifications) (2) Total exposure time (hours) (3) Field size in square arcminute (4) 3 σ limiting Vega magnitude in 1'' aperture as measured on central square arcminute of image (5) Seeing on resultant image.

in less than one pixel difference between all images over the entire field. The K_s and NB 2.07 images of $\mathcal{F}1$ and $\mathcal{F}2$ were merged into one rectangular mosaic image. The overlap in $\mathcal{F}1$ and $\mathcal{F}2$ gives rise to a region of about one square arcminute in the mosaic where the noise level is lowest. As a final step a second set of images was made matching the resolution of the reference image using six stars to estimate the difference in point spread function.

3. Object detection and photometry

3.1. Catalogue sets

The results of the observations and reduction described above are a set of FORS 7' \times 7' images in NB 0.38, *B*, *R* and *I* and a set of ISAAC 2.5' \times 2.5' images in J_s , H , K_s (2 \times) and NB 2.07 (2 \times). From these, we have created catalogs of detected and flux-calibrated objects in order to select (i) objects in K_s band, (ii) EROs, (iii) candidate H α emitters at $z = 2.16$ and (iv) candidate Ly α emitters at $z = 2.16$.

We have used the SExtractor software (v2.2.1, Bertin & Arnouts 1996) for object detection and photometry. Since the background noise level varies across the images as a result of the dithering technique employed, object detection was not performed directly on the final reduced images, but on additional images weighted to give a homogeneous noise level. These were created by multiplication of the reduced images by their associated exposure time maps. Only for the detection of Ly α emitters, a homogeneous noise level image convolved to the *R* band seeing was used, where the detection sensitivity for slightly extended objects (0''.85) is highest. A disadvantage of the use of convolved images for object detection is that spurious sources (e.g. remaining cosmic rays) become indistinguishable from real sources. Three regions in the Ly α detection image that were badly affected by bright stars were blanked (for a total of 7.75 arcminute 2). The source extraction parameters were set so that, detected objects must have at least 8 connected pixels with flux in excess of 1.5 times the background noise level of the detection image, except for the Ly α detection image, where a source

has to have 14 connected pixels. To ensure that the colours are computed correctly, object photometry was done on the convolved images, by employing SExtractor's double image mode using the apertures defined on the weighted images. A weight map created from the square root of the exposure time map was used to estimate the errors in the photometry.

Kron (1980) and Infante (1987) have shown that for stars and galaxy profiles convolved with Gaussian seeing, $> 94\%$ of the flux is inside the appropriately scaled Kron aperture. We have therefore used SExtractor's MAG_AUTO implementation of Kron's first moment algorithm to estimate the *total* magnitudes of the sources. The resultant magnitudes were corrected for galactic extinction of $A_B = 0.172$ (Schlegel et al. 1998) and assuming an $R_V = 3.1$ extinction curve, which resulted in a decrease of the zero-points of B , R and I by 0.2, 0.1 and 0.1 respectively. No changes were necessary for the infrared zero-points.

SExtractor classifies the likelihood of detected objects to be stars or galaxies using a neural network. The resultant *stellaricity* index has a range from 0.0 to 1.0, where stars should have a value near 1.0 and galaxies a value near 0.0.

To derive a list of $H\alpha$ emitting candidates, object detection and aperture definition needed to be done on the infrared narrow band image. For our first set of catalogues, the apertures were therefore defined on the unconvolved homogeneous noise level image associated with the NB 2.07 image. In this way, most remaining cosmic rays and CCD defects are too small to be included in the list and we do not introduce a preference for a fixed spatial frequency. Photometry with these apertures was subsequently carried out on all eight convolved images. The resulting catalogue contains 479 objects, of which thirteen were either spurious or not suitable for the detection of line emitters (e.g. bright stars, a few remaining cosmic rays and some image boundary defects).

We are also interested in the population of EROs in the field of PKS 1138–262. These objects are old elliptical or dusty starburst galaxies at $z > 1$ and may also be present in the proto-cluster structure. EROs have extreme $I - K$ colours, i.e. they are detected in K band but are very faint in the optical. A second set of catalogues was therefore based on the unconvolved homogeneous noise level image associated with the K_s band image. From this set, we derive the K_s band counts and EROs. The resulting catalogue contains 550 objects.

Although candidate $\text{Ly}\alpha$ emitters were selected in Paper I, we have derived a new list of $\text{Ly}\alpha$ candidates based on the newly reduced B and NB 0.38 images using selection criteria consistent with the criteria for selecting the $H\alpha$ emitters presented in this paper. For this purpose, a third set of catalogues was constructed, based on the convolved homogeneous noise level image associated with the NB 0.38 image. This set contains 1027 sources.

Table 3. K_s band galaxy counts

K_s^{lim} (1)	n (2)	N^* (3)	N_{Sco}^* (4)	>4 (5)	>5 (6)
18.0	19	2.5 ± 0.4		1	0
18.5	17	3.8 ± 0.6		6	1
19.0	29	6.2 ± 0.7	4.3 ± 0.3	9	1
19.5	34	8.9 ± 0.8	6.3 ± 0.4	19	2
20.0	58	13.5 ± 1.0	8.4 ± 0.4	26	5
20.5	69	19.0 ± 1.2	11.3 ± 0.5	37	7
21.0	59	23.8 ± 1.4	16.1 ± 0.6	47	11
21.5	84	30.5 ± 1.6		59	16
22.0	55	34.9 ± 1.7		64	19

Notes: (1) Limiting K_s magnitude (2) Differential counts between $K_s^{\text{lim}} - 0.5$ and K_s^{lim} (3) Cumulative number arcmin^{-2} of galaxies brighter than limiting K_s^{lim} , Poisson error is indicated (4) Same as (3) from blank field survey by Scodeggio & Silva (2000) (5) Number of objects brighter than K_s^{lim} with $I - K_s > 4$ (6) Same as (5) for $I - K_s > 5$ (See Sect. 4.2).

4. Number counts and cluster candidates

4.1. K_s number counts

K band number counts were derived from the catalogues based on the K_s image. Table 3 lists the number of sources per half magnitude bin and the cumulative number of sources per square degree. Best (2000, B00 from now on) shows that selecting K band objects with SExtractor's stellaricity index below 0.8 efficiently selects galaxies as opposed to stars. This conclusion is based on the $J - K$ colour of the detected objects which is in general bluer for stars. Because $\mathcal{F}2$ is not imaged in J , we determined the galaxy counts from the total number counts (550 objects) by selecting only those objects with stellaricity index lower than 0.8 (470 objects).

The cumulative counts were compared with observations of a blank field of substantial size (43 arcminute 2) by Scodeggio & Silva (2000). Although these authors also make a distinction between stars and galaxies based on SExtractor's stellaricity index (0.85), it is not clear whether the number counts in their tables are total counts or galaxies only. We assume here that galaxy counts are listed. We observe on average 1.5 ± 0.1 times the number of objects expected from the blank field survey, as illustrated by the observed surface density of galaxies brighter than $K_s = 20$ of 13.5 ± 1.0 arcmin $^{-2}$, compared with 8.4 ± 0.4 arcmin $^{-2}$ determined by Scodeggio & Silva. Less deep, but using a much larger field are the observations of Daddi et al. (2000), which determine a K_s galaxy count of 3.29 ± 0.07 objects arcmin $^{-2}$ up to $K_s = 18.7$ (which is slightly higher than Scodeggio & Silva's value), while we find 4.5 ± 0.6 galaxies arcmin $^{-2}$ up to this limit. From Fig. 2 in Daddi et al. (2000), it is clear that there exist considerable scatter in the observations by different authors, which they interpreted as due to cosmological field-to-field variations of up to a factor two. Our K_s band counts are near the upper limit of the observed variations.

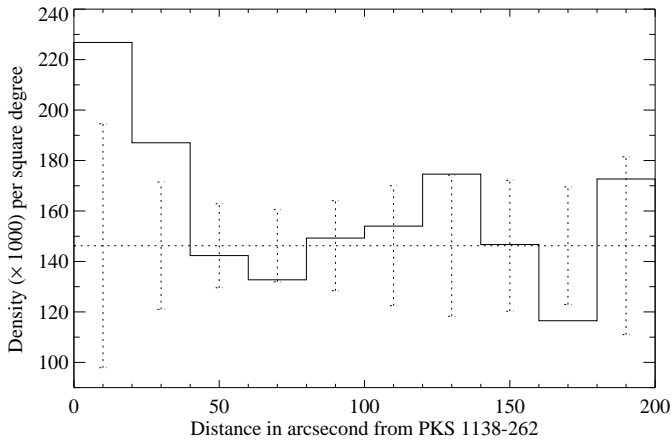


Fig. 1. Galaxy counts as a function of distance from the radio galaxy in circular bins of $20''$ width. The error-bars represent Poissonian errors. The mean density (146×1000) per square degree inside the largest circle ($210''$, bin not shown) is indicated by the horizontal line.

We have analyzed the surface density of K band selected galaxies as a function of distance from the radio galaxy by counting the number of galaxies in circular areas around 1138–262. Fig. 1 shows the number of galaxies per arcsecond 2 in circular bins of $20''$. It is clear that the counts show an excess within $50''$ or 0.45 Mpc from the radio galaxy. The deviation from the mean density of the joined first two bins is 2.2σ .

The richness of clusters can be assessed by counting the number of cluster galaxies found within a radius of 0.5 Mpc of the central galaxy with magnitudes between m_1 and m_1+3 , m_1 being the magnitude of the central galaxy. This value, $N_{0.5}$, is defined by Hill & Lilly (1991) and based on an earlier definition by Abell (1958). The K magnitude measured for 1138–262 is 16.1. We can correct this value for line emission from $\text{H}\alpha$ and NII as measured in the NB 2.07 band, by solving for line and continuum contributions in the broad and narrow band. We obtain

$$c = \frac{b - n}{\Delta\lambda_{\text{bb}} - \Delta\lambda_{\text{nb}}}, \quad (1)$$

where c , b and n are the continuum flux and flux measured in broad and narrow band and $\Delta\lambda_{\text{bb}}$, $\Delta\lambda_{\text{nb}}$ are the FWHM of the broad and narrow band, respectively. The K magnitude in the NB 2.07 band is 15.8 and the resulting magnitude of the continuum flux therefore 16.2. Note that this difference of 0.1 units of magnitude is less than the 0.3 units derived in Pentericci et al. (1997) based on an assumed $\text{Ly}\alpha/\text{H}\alpha$ ratio of 1. In addition to line flux, we have to correct for other non stellar contributions. Pentericci et al. (1997) attribute 0.2 magnitude units to the point source contribution and a maximum of 0.2 units to the resolved contribution. We conclude that the continuum K magnitude representative of the stellar population in the brightest cluster galaxy is close to 16.5. At $z = 2.16$, 0.5 Mpc is equivalent to $56''$, and the angular area occupied by a disc with 0.5 Mpc radius is 2.7 arcmin 2 .

The number of galaxies between 16.5 and 19.5 in this area around 1138–262 is 31. From Table 1 in B00, we find that blank fields contain $\sim 2.06 \times 10^4$ galaxies per square degree between magnitude 16.5 and 19.5 (references to the blank field data can be found in the caption of Fig. 6 in B00), or 15 galaxies within a circular area of $56''$ radius. The net excess count around 1138–262 is therefore 16 ± 6 . From Table 4 in Hill & Lilly (1991) we read that for clusters of richness 0, 1, 2, the mean $N_{0.5}$ values determined by Bahcall (1981) are 12 ± 3 , 15 ± 5 , 29 ± 8 . The mean value of $N_{0.5}$ in 3C radio galaxy fields (Yates et al. 1989) is 11 ± 2 , similar to the average number of 11 galaxies in the 28 $z \sim 1$ radio galaxy fields found by B00. The measured $N_{0.5}$ suggests that 1138–262 is located in an environment with a density comparable to richness class 0 or 1 clusters. During the evolution of this structure, however, more galaxies might fall in, further increasing the richness of the cluster.

4.2. Extremely red objects

Since the discovery of extremely red objects (EROs, Elston et al. 1988, 1989), there has been considerable interest for these high redshift galaxies because their properties can constrain models of galaxy formation and evolution. They are now generally believed to be either evolved ellipticals or dusty starbursts at $z > 1$ and have been shown to cluster strongly (Daddi et al. 2000). Using our multi band observations, we can search for EROs which could form a population of galaxies associated with the radio galaxy at $z \sim 2.16$. Clusters are known to possess a population of elliptical galaxies which form a *red sequence* in a colour-magnitude diagram (e.g. Bower et al. 1992). The evolution of the elliptical galaxy population in clusters has been shown by numerous authors (e.g. Stanford et al. 1998) to be simple and homogeneous, indicating that the stellar population that makes up the red sequence is formed at high redshifts ($z_f > 2$). Gladders & Yee (2000) show that the red sequence can be exploited to find clusters of galaxies up to $z \sim 1.4$ using optical imaging. Basically, the cluster red sequence is as red as or redder than other galaxies at a given redshift and all lower redshifts if properly chosen filters straddling the 4000 Å break are used (Gladders & Yee 2000). For a cluster elliptical at $z = 2.2$ the 4000 Å break is redshifted to 12800 Å, in the infrared J band. We have selected EROs based on their $I - K_s$ colour, which also targets galaxies at the redshift of the proto-cluster. The samples selected with these bands can be compared with literature data.

4.2.1. EROs in the field of PKS 1138–262

Figs. 2 and 3 show plots of $I - K$ vs K and $I - K$ vs $J - K$ for the sources with apertures defined on the K_s band image. These plots show that there is a considerable number of objects with very red colours ($I - K_s > 4$) in our field. An enlargement of Fig. 3 is shown in Fig. 4 for the

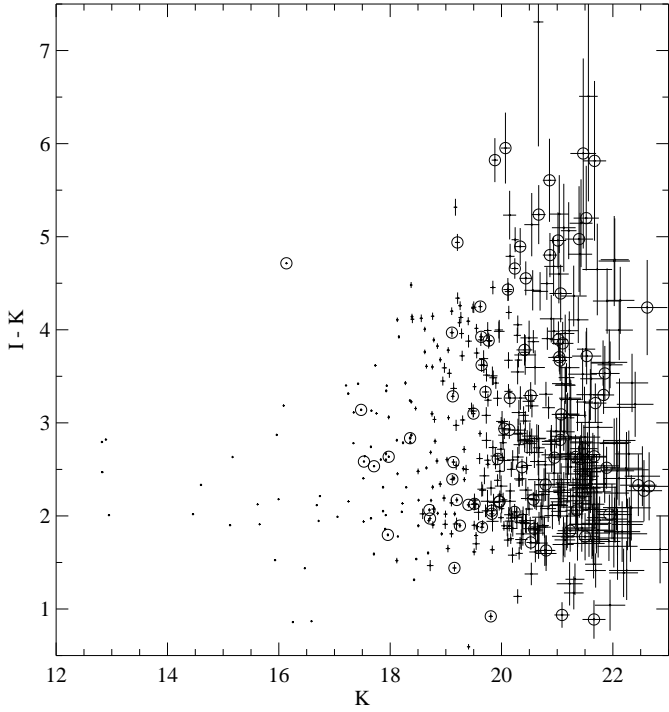


Fig. 2. Colour-magnitude plot of $I - K$ vs K for the 544 sources detected on the K_s band image. The sources within $40''$ of the radio galaxy are indicated by circles.

range in $I - K > 3.75$. For $I - K > 4.3$, there are very few bright objects: the median K band magnitude in the range $4.3 < I - K < 5.1$ is 20.9 while it is 1.3 magnitude lower in the range $3.5 < I - K < 4.3$, with the sole exception of the radio galaxy ($I - K = 4.8$, $J - K = 2.8$). This increase in magnitude suggests that a large fraction of the objects redder than this limit are distant galaxies and we consider therefore the 44 objects with $I - K > 4.3$ in the field of 1138–262 as EROs for the remainder of this paper. These objects are listed in Table A.3. However, since other authors use different criteria, we have listed the number of red objects according to several selection criteria in Table 4.

We will compare the number density of EROs in the field of 1138–262 with the density observed in a 23.5 arcmin 2 area of the *Chandra* Deep Field by Scoville & Silva (2000), which agrees well with the density of $I - K_s > 4.0$ objects measured by Cowie et al. (1996). In Table 3, the number of objects with $I - K > 4$ and > 5 found in the field of 1138–262 is shown per K_s magnitude limit. Up to $K_s = 21$, one expects 33 ± 4 (6 ± 2) EROs with $I - K > 4$ (5) in a blank field of this size, while we observe 47 (11). Note, however that Daddi et al. (2000) claim that the density of EROs with $R - K_s > 5$ and $K < 19$ in the 43 arcmin 2 CDFS, derived by Scoville & Silva (2000), is a factor of five smaller than the one derived in the 700 arcmin 2 survey by Daddi et al. (2000). This large discrepancy is not unexpected given the strong clustering of EROs. Although we are using different selection criteria and most EROs

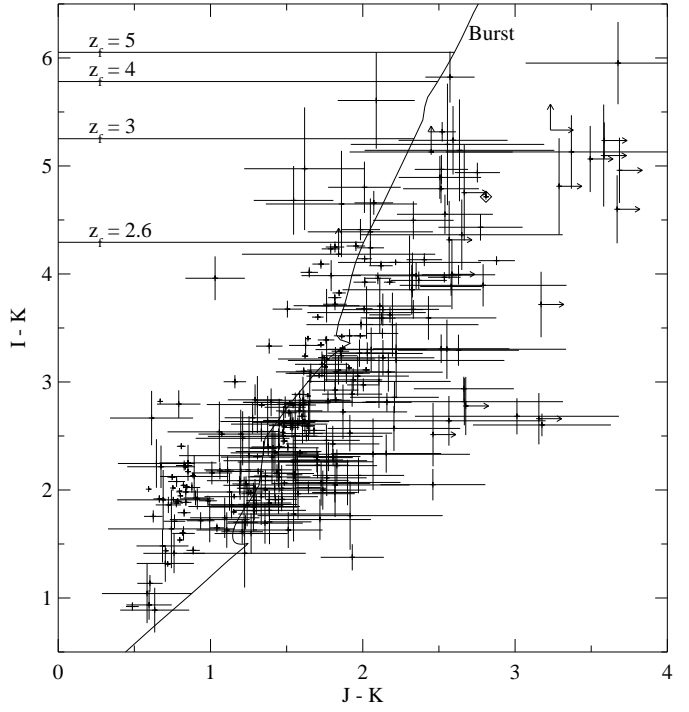


Fig. 3. $I - K$ vs $J - K$ colour-colour plot for the 320 sources detected in the central K_s band image. Non-detections in I or J and therefore lower limits on the magnitude are indicated by arrows. The radio galaxy (indicated by a diamond) has $J - K = 2.8$ and $I - K = 4.7$. The track marks the colour of a stellar population at $z = 2.2$ formed by a 100 Myr single burst followed by passive evolution for ages of 0.5 Myr to 2.4 Gyr after the burst. Four formation redshifts of the population are indicated. PKS 1138–262 is indicated by a diamond.

detected in our comparatively small 12.5 arcmin 2 field are fainter than $K = 19$, we should be careful drawing conclusions from this comparison. It is unclear whether the clustering of EROs at fainter flux levels is as strong as at bright levels, but the measurements by Daddi et al. (2000) show that the clustering amplitude of EROs with $K_s < 18.5$ is twice as high as of EROs with $K_s < 19.2$. Eqs. 8 and 9 in Daddi et al. (2000) prescribe the rms fluctuation of ERO counts due to cosmic variance, given the clustering strength of EROs. We have made the conservative assumption that $K = 21$ EROs are clustered as strongly as $K = 19$ EROs, resulting in an uncertainty on the number of EROs with $I - K > 4$ (5) of 11 (4). Therefore, we tentatively find an over-density of about a factor of 1.5, which might be due to a population of EROs in the proto-cluster at $z \sim 2.2$ on top of a field population of EROs at lower redshift.

An important argument for the proposition that part of the ERO population consists of proto-cluster members at $z = 2.2$ is the gradient in the spatial distribution of EROs, as shown in Fig. 5, which is similar to the distribution of K_s band counts. The density within a $40''$ radius of the radio galaxy is more than four times higher than the

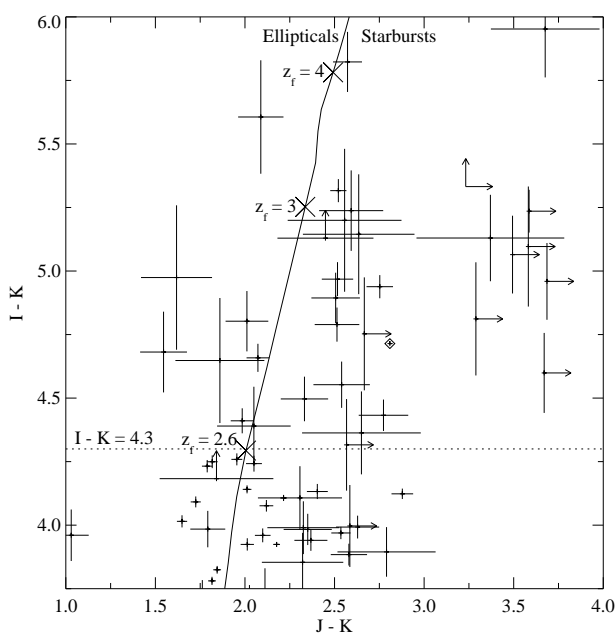


Fig. 4. This close-up of Fig. 3 shows the extremely red objects. The horizontal line denotes our ERO selection criterion $I - K > 4.3$. Error-bars have been reduced in size by a factor two to increase the readability of the plot. The solid line, diamond and arrows are described in the caption of Fig. 3. Three formation redshifts for the stellar population are indicated.

Table 4. Extremely Red Objects counts near PKS 1138–262

$I - K$	#	#C
(1)	(2)	(3)
4.3 - 5.3	36	27
> 5.3	8	6
4.5 - 5.5	25	22
> 5.5	7	5

Notes: (1) $I - K$ colour (2) Number of EROs in 12.5 arcmin^2 field covered by both K band images (3) Number of EROs in 7.1 arcmin^2 field covered by central K_s band image only.

mean density outside a $60''$ (0.5 Mpc) radius. This mean surface density of 8×10^3 galaxies per square degree would imply a number of 28 EROs in the field, roughly consistent with the number expected from the blank field observed by Scudegger & Silva (2000). In Fig. 2, the objects within $40''$ from the radio galaxy are indicated by circles. It is clear that many of the reddest objects lie near the radio galaxy: there are 17 EROs within a $40''$ radius of 1138–262 (12 arcmin^{-2}) and 27 outside this radius (2.4 arcmin^{-2}). The over-density of EROs in the field of 1138–262 is therefore mostly due to the red galaxies near the radio galaxy, which is consistent with the observed excess of EROs being due to a cluster population associated with the radio galaxy.

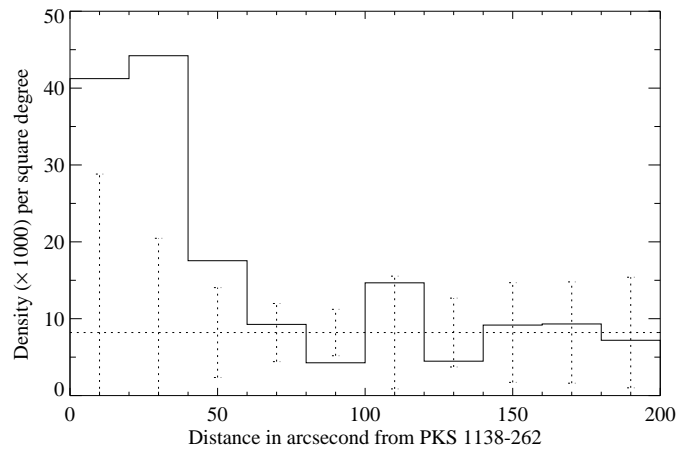


Fig. 5. Extremely red object ($I - K > 4.3$) counts as a function of distance from the radio galaxy. The EROs are counted in circular bins of $20''$ width. The error-bars represent Poissonian errors. The mean density (8×1000) per square degree outside $60''$ (0.5 Mpc) is indicated by the horizontal line.

4.2.2. EROs in the proto-cluster at $z = 2.2$

What colours do we expect for galaxies at $z = 2.2$? We have computed evolutionary tracks for several stellar population using the Galaxy Isochrone Synthesis Spectral Evolution Library (GISSEL93, Bruzual & Charlot 1993). The IMF we have used in the models is a Salpeter (1955) law with lower mass cutoff at $0.1 M_\odot$ and upper mass cutoff at $125 M_\odot$. On Fig. 3 a track is indicated for a stellar population at $z = 2.2$ formed by passive evolution after a 100 Myr single burst model. The track starts at an age of 5 Myr at $I - K = 0.5$ and leaves the plot at an age of 2.4 Gyr ($I - K = 6.5$). We have also computed the colours for a constant star formation model, and an exponential star formation model with $\tau = 1$ Gyr, but these did not reach $I - K > 4$ even after 4 Gyr, the maximum age for a galaxy at $z = 2.2$ in this cosmology. The EROs in the field of 1138–262 have colours consistent with galaxies which have undergone a starburst 0.5 Gyr ago ($z = 2.6$) or longer and evolved passively thereafter. However, dust reddening is not taken into account in the models presented here. Reddening of actively star forming galaxies by dust can also shift their $I - K$ colours into this regime as shown by e.g. Pozzetti & Mannucci (2000). The $I - K$ colour of their elliptical template increases to ~ 7 at $z > 2$, while the colour of their dusty starburst template stays constant at ~ 6 . We observe no objects with $I - K \sim 7$, but there are three objects with lower limits to their $I - K$ colour of ~ 6 , which could be $z \sim 2$ ellipticals and a few objects with $I - K \sim 6$. We conclude that the excess of $\sim 10 - 15$ of the EROs in the field of 1138–262 is caused mostly by galaxies at $z = 2.2$ which are reddened by dust.

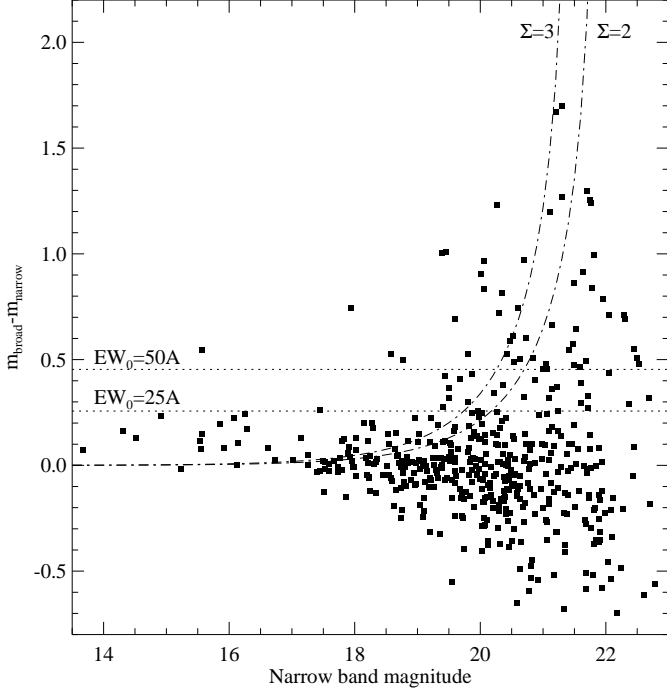


Fig. 6. Colour-magnitude diagram for 467 sources detected in the NB 2.07 image. The dot-dashed lines are lines of constant excess signal Σ (see text). Also shown are lines of constant EW_0 (for $z = 2.16$). Candidate $H\alpha$ emitters are objects with $EW_0 > 25$ or 50 Å and $\Sigma > 2$ or 3 (see table 5).

4.3. Candidate $H\alpha$ emitters

4.3.1. Selection procedure

Candidate line emitting objects were selected on the basis of their excess narrow versus broad band flux, following the criteria of Bunker et al. (1995) and Moorwood et al. (2000). The selected candidates fulfill two criteria: first, they have sufficient equivalent width (EW) and second, their broad band flux is significantly lower than expected for a flat spectrum source. Having measured the narrow band flux for each source, we compute the expected broad band flux and its standard deviation assuming a flat spectrum. The error parameter Σ is defined as the number of standard deviations the measured broad band flux deviates from the expected broad band flux of a flat spectrum source (see also Bunker et al. 1995). Note that Σ is well defined for objects not detected in the broad band. A NB 2.07 – K_s band versus NB 2.07 magnitude plot for the 466 bona fide objects in the $H\alpha$ selection catalog (see Sect. 3) is shown in Fig. 6. Also drawn are two horizontal lines indicating rest frame equivalent width (EW_0) of 25 and 50 Å and two curves indicating Σ equal to 3 and 2. The curves of constant Σ have been computed for median narrow band and broad band errors; the actual Σ of individual sources depends, amongst others, on the aperture size and local background noise.

Table 5. Properties of the samples of $H\alpha$ candidates

EW_0 (1)	Σ (2)	m_{NB} (3)	# (4)	#H (5)	n_{1138} (6)	n (7)
50	3	–	17	2	1.4 ± 0.3	
25	3	–	23	3	1.8 ± 0.4	
25	2	–	40	3	3.2 ± 0.5	
50	1	–	48	2	3.8 ± 0.6	
25	1	–	60	3	4.8 ± 0.6	
75	2	19.3	1	0	0.1 ± 0.1	0.61 ± 0.35^a
100	3	19.5	2	1	0.2 ± 0.1	0.12 ± 0.05^b

Notes: (1) Rest frame equivalent width lower limit (2) Signal to noise lower limit (as defined by Bunker et al. 1995) (3) Additional selection criterion: narrow band magnitude upper limit (4) Number of candidates in 12.5 arcmin^2 area (5) Number of candidates within the radio galaxy $Ly\alpha$ halo (6) Surface density of candidates in the field of $1138-262$ (arcmin^{-2}) (7) Surface density in other fields: ^a Bunker et al. (1995), ^b van der Werf et al. (2000).

We find 17 candidate emitters with rest-frame equivalent width $EW_0 > 50$ Å and $\Sigma > 3$, all of which have narrow band magnitudes ≤ 21.3 . One of these objects is the radio galaxy, while a second is within the extent of the $Ly\alpha$ halo of the radio galaxy. If we lower the selection criteria to $EW_0 > 25$ Å and $\Sigma > 2$, we find 40 candidates. All of these have $m_{NB, 2.07} \leq 21.6$. In addition to the two objects identified above, there is one more object in this list within the radio galaxy $Ly\alpha$ halo. The $H\alpha$ halo of the radio galaxy is interesting in itself, especially in comparison with the $Ly\alpha$ halo and will be studied in another article (Kurk et al. in preparation). Table 5 lists the number of candidates in both fields for several selection criteria, while Table A.1 lists the K magnitude and emission line properties, for the candidates with $EW_0 > 25$ Å and $\Sigma > 2$. The NB 2.07 narrow band filter used also includes the $[\text{N II}]\lambda\lambda 6548, 6584$ Å lines at $z = 2.16$, but in what follows, we will refer to the combined $H\alpha + \text{N II}$ flux and equivalent width, as $H\alpha$ flux and equivalent width respectively, unless otherwise noted.

4.3.2. Number density of candidate $H\alpha$ emitters

In recent years the number of successful searches for $H\alpha$ emitters in the infrared has grown. Bunker et al. (1995) have obtained near infrared narrow band images in a 4.9 arcmin^2 field towards the quasar PHL 957, in an attempt to detect $H\alpha$ emission from a damped $Ly\alpha$ absorber at $z = 2.313$. They find 3 candidate $H\alpha$ emitters at $2.29 < z < 2.35$ with $EW_0 > 75$ Å and $\Sigma > 2$, brighter than a narrow band magnitude limit of 19.3. More recently, van der Werf et al. (2000) presented a survey for $H\alpha$ emission at redshifts from 2.1 to 2.4. They have observed several fields containing known damped $Ly\alpha$ systems (also including the field of PHL 957) and radio galaxies as well as random fields for a total area of 55.9 arcmin^2 . They detect two radio galaxies and a

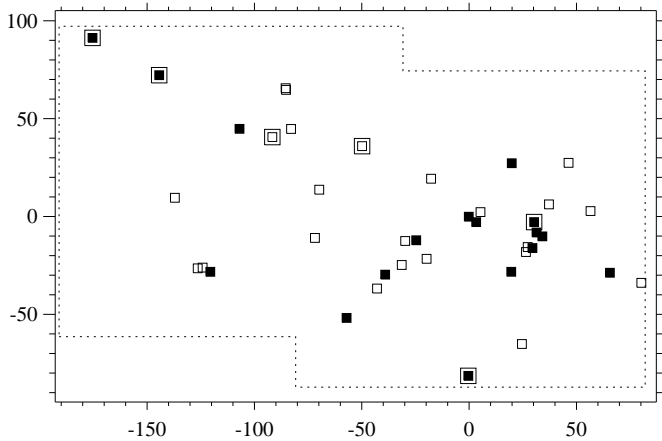


Fig. 7. Position plot for the 40 (17) $\text{H}\alpha$ candidates with $\text{EW}_0 > 25$ (50) \AA and $\Sigma > 2$ (3) indicated by open (filled) squares. Large squares indicate candidates for which $\text{Ly}\alpha$ emission has been detected (see Sect. 5.1). Axes are in arcseconds, the radio galaxy is at the origin. The dotted boxes indicate the borders of the two reduced ISAAC fields.

damped $\text{Ly}\alpha$ absorber in the field of PHL 957 in $\text{H}\alpha$ emission accompanied by two close emitters which had not been observed before. In addition, they find another candidate in the field of a radio galaxy, but at a large distance from it ($81''$), which seems to be a merging galaxy. In total, they find seven $\text{H}\alpha$ emitters with $\text{EW}_0 > 100 \text{\AA}$ and $\Sigma > 3$ down to an area weighted narrow band magnitude limit of 19.5. The narrow band fluxes of these candidates are $> 2.0 \times 10^{-16} \text{ erg cm}^{-2} \text{ s}^{-1}$.

Our VLT near infrared imaging is much deeper and most of our candidates have fluxes below this limit. To compare the number density of $\text{H}\alpha$ emitters in our field with the above mentioned authors, we have done the selection according to their limits, including the lower narrow band magnitude limits imposed by their shallower observations. We find only one and two candidates (see Table 5), resulting in number densities (with large Poisson errors) slightly lower and higher than Bunker et al.'s and van der Werf et al.'s surveys, respectively.

4.3.3. Spatial distribution

Fig. 7 shows the spatial distribution of candidate $\text{H}\alpha$ emitters. This distribution is not homogeneous over the observed fields. To quantify this inhomogeneity, we have counted the number of candidates with $\text{EW}_0 > 25 \text{\AA}$ and $\Sigma > 2$ in circular bins of $20''$ radius around the radio galaxy. We have taken into account the variation in sensitivity per pixel using the weight map associated with the NB 2.07 image. This alters the density per bin by less than 20% in all bins compared with the unweighted computation. The $\text{H}\alpha$ candidate selection depends also weakly on the K_s band sensitivity, but we do not expect this to have a large influence on the density per bin and certainly not on the conclusions from this plot. The density within a $40''$ distance of the radio galaxy is 5.0 ± 0.9 times higher

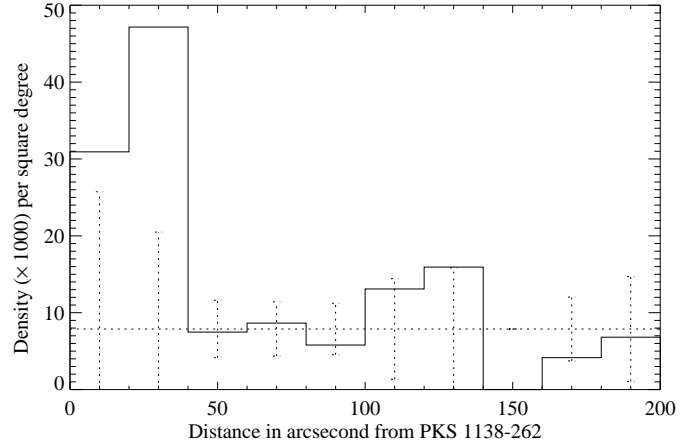


Fig. 8. Candidate $\text{H}\alpha$ emitter ($\text{EW}_0 > 25 \text{\AA}$, $\Sigma > 2$) counts as a function of distance from the radio galaxy. The candidates are counted in circular bins of $20''$ width. The error-bars represent Poissonian errors. The mean density (7.9×1000) per square degree outside 1 arcminute (0.5 Mpc) is indicated by the horizontal line.

than the mean density outside a $60''$ (0.5 Mpc) radius. The high number of candidates near the radio galaxy is consistent with 1138–262 being located in a region that is over-dense in $\text{H}\alpha$ emitting galaxies.

4.3.4. Contamination by other line emitters

We do not expect that a significant fraction of our emission line candidates are line emitters at lower redshift, since there are no strong emission line redward of $\text{H}\alpha$ at 6563\AA ($\text{Pa}\alpha$ with a strength ~ 0.2 times the strength $\text{H}\alpha$ would imply $z = 0.1$). It is possible that we have selected galaxies at $z \sim 3.13$ with strong $[\text{O III}]\lambda 5007 \text{\AA}$ emission or galaxies at $z \sim 4.55$ with $[\text{O II}]\lambda 3727 \text{\AA}$ emission. The luminosity distance for objects at $z \sim 4.6$ is 2.5 times larger than for objects at $z \sim 2.16$. If any of the emitters is indeed an $[\text{O II}]$ emitter at this redshift, its intrinsic luminosity is six times higher than that assumed for $\text{H}\alpha$ in Table A.1. It is therefore unlikely that these objects contaminate our sample significantly. More likely is the contribution of $[\text{O III}]$ emitters to our sample, illustrated by follow-up spectroscopy to narrow band observations similar to ours. All six galaxies suspected to be $\text{H}\alpha$ emitters at $z \sim 2.2$ from low signal-to-noise near-infrared spectroscopy by Moorwood et al. (2000) were found to be $[\text{O III}]$ emitters at higher redshift when observed at high enough signal-to-noise to detect the $[\text{O III}]\lambda 4959 \text{\AA}$ line (P. van der Werf, private communication). Although on the basis of the present data, we cannot separate $\text{H}\alpha$ emitters at $z \sim 2.2$ from line emitters at higher redshift, the spatial distribution of the candidate $\text{H}\alpha$ emitters indicates that at least ~ 12 are associated with the radio galaxy and are therefore bona fide $\text{H}\alpha$ emitters surrounding the cluster. There is, however, one candidate which stands out by its brightness ($K = 17.7$) and its size ($\sim 3''$) from the others ($K \geq 19.3$). The narrow band excess emission from

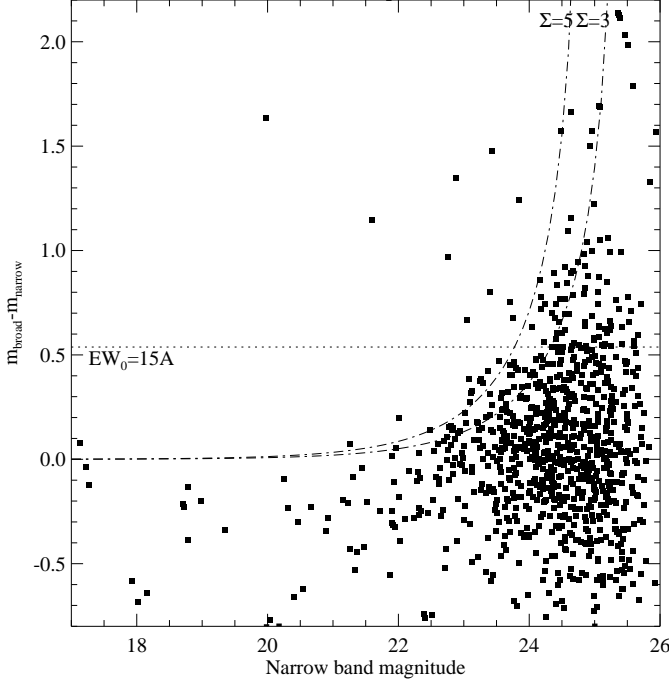


Fig. 9. Colour-magnitude diagram for 1018 sources detected in the NB 0.38 image. The dot-dashed lines are lines of constant Σ (see text). Also shown is a line of constant rest frame equivalent width (for $z = 2.16$). Candidate Ly α emitters are objects with $EW_0 > 15 \text{ \AA}$ and $\Sigma > 3$ or 5.

this candidate is most likely caused by Pa α emission at $1.875 \mu\text{m}$ redshifted to $z = 0.104$ and marked as such in Table A.1.

4.4. Ly α candidates

4.4.1. Selection procedure

Using the catalogue with apertures based on the convolved and partly blanked NB 0.38 image, candidate Ly α emitting objects were selected on the basis of excess narrow versus broad band fluxes, similar to the method used to select H α candidate emitters. Seven spurious objects near the edges of the images, one saturated star and one blended object were removed from the catalogue. The difference between the narrow and broad band magnitude for the 1018 definite objects is plotted in Fig. 9. A horizontal line indicates rest frame equivalent width (EW_0) of 15 \AA and curves are drawn for Σ equal to 5 and 3. The curves of constant Σ have been computed for median narrow band and broad band errors; the actual Σ of individual sources depends, amongst others, on the aperture size and local background noise. We find 11 candidate emitters with rest-frame equivalent width $EW_0 > 15 \text{ \AA}$ and $\Sigma > 5$. If we lower the signal-to-noise criterion to $\Sigma > 3$, we find 40 candidates (see Table A.2). One of these objects is the radio galaxy, while two more are also within the extent of the Ly α halo of the radio galaxy. We have checked the num-

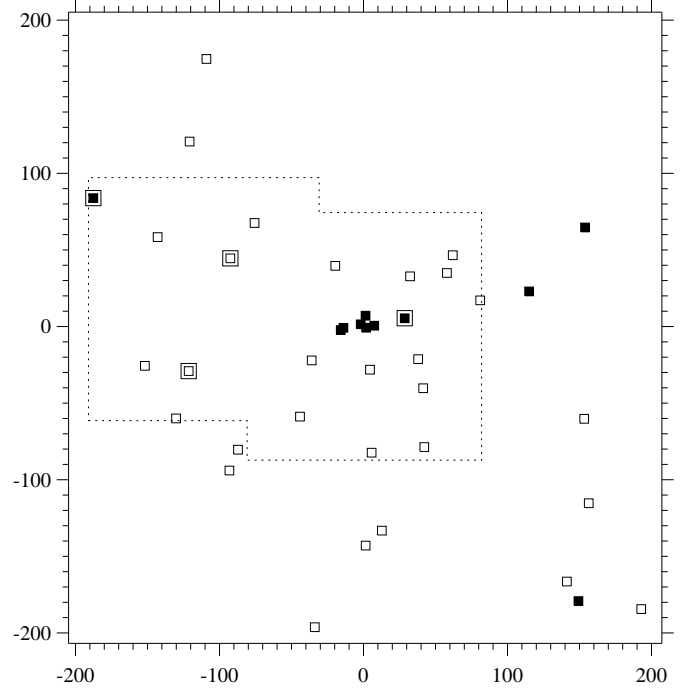


Fig. 10. Position plot for the 40 (11) Ly α candidates with $EW_0 > 15 \text{ \AA}$ and $\Sigma > 3$ (5) indicated by open (filled) squares. Large squares indicate candidates for which H α emission has been detected (see Sect. 5.1). Axes are in arcseconds, the radio galaxy is at the origin. The dotted boxes indicate the borders of the two reduced ISAAC fields.

ber of candidates which would be selected out of the new catalogues using the criteria used in Paper I ($EW_\lambda > 65 \text{ \AA}$ and $\mathcal{F}_{\text{NB}0.38} > 2 \times 10^{-19} \text{ erg cm}^{-2} \text{ s}^{-1} \text{\AA}^{-1}$). We find 70 candidates, which is consistent with the 60 candidates found in Paper I, given that the image on which the current selection is done is $\sim 24\%$ larger than the image on which the catalogue of Paper I was based.

4.4.2. Spatial distribution

Fig. 10 shows the spatial distribution of the Ly α candidate emitters. In the south east corner of the image is a bright star and a nearby galaxy which inhibits the detection of any faint Ly α emitters. Although the distribution of the candidates is not homogeneous, there is not a strong indication of a density concentration within $40''$ of the radio galaxy, but at distances $> 120''$ the density is somewhat below the mean, as Fig. 11 shows. The first bin in this plot contains six objects: the radio galaxy, three objects which are part of the filamentary Ly α halo and two more which might be associated to the halo. Most other bins are consistent with the mean density of 3.4×1000 candidates per degree 2 .

4.4.3. Number density of candidate Ly α emitters

To determine the galaxy over-density near PKS 1138–262, we would like to compare the number density of Ly α emit-

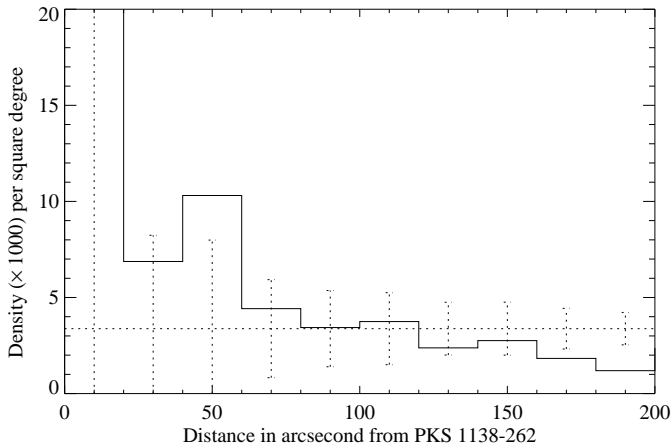


Fig. 11. Candidate Ly α emitter ($\text{EW}_0 > 15 \text{ \AA}$, $\Sigma > 3$) counts as a function of distance from the radio galaxy. The candidates are counted in circular bins of $20''$ width. The error-bars represent Poissonian errors. The mean density (3.4×1000) per square degree is indicated by the horizontal line.

ters found in our field to the number density of Ly α emitters in a blank field. In recent years, a number of surveys for Ly α emitting objects at high redshift have or are being carried out. The utility of Ly α selected galaxies, representing the faint end of the galaxy luminosity function, as tracers of large scale structure was illustrated by Fynbo et al. (2001). The redshifts and positions of eight objects at $z \sim 3.0$ found by their Ly α emission (Fynbo et al. 2000) are consistent with this structure being a single string spanning about 5 Mpc, the first signal observed of a filament at high redshift (Møller & Fynbo 2001). Larger surveys have been carried out at higher redshifts: 3.4 (Hu et al. 1998), 4.5 (Hu et al. 1998; Rhoads et al. 2000), 4.9 (Ouchi et al. 2002) and 5.7 (Rhoads & Malhotra 2001). One of the notable results of these surveys is that the observed equivalent widths of the Ly α emitters indicate that they are young galaxies undergoing their first burst of star formation. There are currently no observations available of Ly α emitters at $z \sim 2.2$ in a blank (or any other) field, although such a survey is underway at the Nordic Optical Telescope which has the necessary but rare high UV throughput (e.g. Fynbo et al. 2002). We will therefore compare our results to the observations of a known over-density of LBGs at $z = 3.09$ imaged in Ly α (Steidel et al. 2000, S00 from now on) and a shallower but much larger survey at $z = 2.42$ (Stiavelli et al. 2001), assuming that the results obtained at higher redshift are also applicable at $z = 2.2$. This assumption seems to be justified by the conclusion of Yan et al. (2002) that the galaxy luminosity function does not evolve significantly from $z \sim 3$ to $z \sim 6$ and by the observation of Ouchi et al. (2002) that the Ly α and UV-continuum luminosity functions of Ly α emitters show little evolution between $z = 3.4$ and $z = 4.9$.

S00 have selected a sample of 72 bona fide line excess emitters with a narrow band magnitude limit of $\text{NB}_{\text{AB}} = 25.0$ and observed frame equivalent width ($\text{EW}_\lambda > 80 \text{ \AA}$.

This magnitude limit corresponds to $\text{NB} 0.38 = 24.3$. The number of Ly α candidates in the effective 43.6 arcmin^2 field of 1138–262 with $\text{EW}_\lambda > 80 \text{ \AA}$ and $\text{NB} 0.38 < 24.3$ is 11. The surface density of these objects is 0.25 arcmin^{-2} , about a fourth of the value (0.96 arcmin^{-2}) measured by S00. Taking into account the redshift range of detectable Ly α emitters corresponding to the FWHM of the NB 0.38 filter gives a comoving volume density of 0.0011 Mpc^{-3} . The 72 candidates detected by S00 are located in a comoving volume of 21041 Mpc^3 in our cosmology, resulting in a volume density of 0.0034 Mpc^{-3} . The overdensity of galaxies at $z = 3.09$ is a factor six, consistently determined by S00 from the redshift density of LBGs as compared with the general LBG redshift distribution and from the comoving volume density of the Ly α candidates at $z = 3.09$ compared to a blank field survey at $z = 3.43$ (Cowie & Hu 1998). Since the comoving volume density of candidate Ly α emitters in our field is 3.1 times smaller than the density found by S00, we estimate the galaxy overdensity in the field of PKS 1138–262 to be a factor 2 ± 1 . A more direct comparison with Cowie & Hu (1998) also gives a volume overdensity of 1.6 ± 0.7 . The quoted errors are derived from the Poisson noise on the number of emitters in the three fields, but the uncertainty due to the difference in blank field number density at $z \sim 2.2$ and $z \sim 3.1, 3.4$ might be larger.

Stiavelli et al. (2001) have carried out a search for Ly α emitters in a field of 1200 square arcminutes using a medium band filter and found 58 candidates at $z = 2.4$. Since this sample has on average a red colour ($< B - I > = 1.8$), they conclude that the emitters contain an older stellar component and have therefore undergone their major episode of star formation at higher redshift. The 58 candidates have continuum subtracted narrow band fluxes $> 2.0 \times 10^{-16} \text{ erg cm}^{-2} \text{ s}^{-1}$. Taking into account the difference in luminosity distance, we find 3 candidates with fluxes $> 2.6 \times 10^{-16} \text{ erg cm}^{-2} \text{ s}^{-1}$ in the field of 1138–262. This amounts to a surface density of $0.07 \text{ candidates arcmin}^{-2}$, about a factor two more than the $0.048 \text{ sources arcmin}^{-2}$ found by Stiavelli et al. The 4% filter used in their survey implies a comoving volume of $7.6 \times 10^5 \text{ Mpc}^3$ and a comoving volume density of $7.6 \times 10^{-5} \text{ Mpc}^{-3}$, while the 8 candidates near 1138–262 yield a comoving volume density of $3.1 \times 10^{-4} \text{ Mpc}^{-3}$. The overdensity implied by the difference in comoving volume density is a factor 4 ± 2 . Although we have not corrected our sample of candidate Ly α emitters for low redshift interlopers, it is evident that the field of 1138–262 contains an overdensity of emitters with respect to blank field. In Sect. 6.2 we discuss the overdensity of the Ly α emitters with confirmed redshifts and estimate the mass of the proto-cluster implied.

4.5. Coincidence of Ly α and H α emitters and EROs

We have now identified candidate cluster members on the basis of three different criteria and we are able to find

Table 6. Overdensities of the three samples

R ₁₁₃₈	< 40''		< 60''		20''–60''		
	(1)	(2)	(3)	(2)	(3)	(2)	(3)
EROs	4.7	2.5	3.2	2.9	3.3	3.3	
H α	4.8	2.6	2.6	2.5	2.8	3.0	
Ly α	2.6	1.0	3.1	1.5	3.1	1.7	

Notes: (1) Sample, either EROs, candidate Ly α or H α emitters
 (2) Density in terms of background density (3) Significance (σ) of (2).

out whether there is any overlap between the three populations in the area covered by the infrared imaging. The radio galaxy fulfills all requirements: it is an extremely red object with both Ly α and H α emission. The extended emission line halo also contains several objects which are found to be either EROs, H α or Ly α emitters. Apart from the radio galaxy, there are two objects classified both as ERO and candidate H α emitter. One of these is located in the central infrared field where a J magnitude is available and is placed within the starburst region defined by Pozzetti & Mannucci (2000). The H α emitting EROs have $I-K$ magnitude ~ 4.4 . There are no candidate Ly α emitters with $I-K$ colour red enough to be classified as EROs. This is consistent with the idea that the EROs are dusty starbursts (Dey et al. 1999) for which we do not expect Ly α emission due to the strong extinction but at least some H α emission. There are several groups of EROs, H α and Ly α emitters close together, as can be seen in Fig. 12. None of the candidate Ly α or H α emitters have sufficient infrared or optical narrow band excess emission to be selected as a H α or Ly α candidate, respectively. A more elaborate discussion of Ly α /H α ratios of the candidate emitters is postponed to Sect. 5.1.

4.6. Comparison of the spatial distributions

It seems (Figs. 5, 8, 11) that the H α candidates and EROs are more concentrated towards 1138–262 than the Ly α emitters. To determine whether these differences are significant, we compare the concentration of galaxies towards the radio galaxy by measuring the height and width of the density peak on top of the background population. We define the surface density of the background population as the density at 60'' (0.5 Mpc) $< R_{1138} < 200''$ (1.8 Mpc), where R₁₁₃₈ is the distance from the radio galaxy. The height of the peak within certain values of R₁₁₃₈ is given in Table 6 along with its significance σ . For this computation we have excluded the radio galaxy halo objects. It is clear that the density peaks of the EROs and H α candidates are more significant than of the Ly α candidates for all R₁₁₃₈ $< 60''$. The former peaks are also more pronounced at short distances (R₁₁₃₈ $< 40''$), i.e. their width is smaller. We conclude that there is good evidence that the EROs and candidate H α emitters are more concentrated towards PKS 1138–262 than the candidate Ly α emitters.

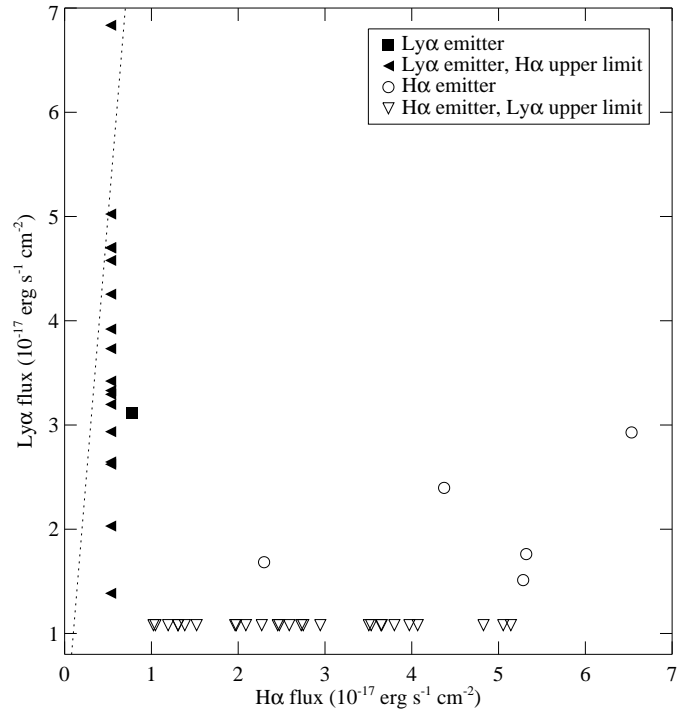


Fig. 13. Ly α vs H α flux for candidate Ly α emitters (filled symbols) and H α emitters (open symbols). Triangles indicate upper limits. The dotted line indicates a Ly α /H α ratio of 10, approximately the case B prediction.

5. Properties of the candidates

5.1. Ly α /H α ratios of the candidate emitters

There are no objects selected as both Ly α and H α candidates, but for some candidates we have detected emission in the other line below the selection criteria used in this work. The small overlap might seem surprising at first since both lines are produced by the recombination of neutral hydrogen. However, the strength of the H α line is about a factor of ten less than the Ly α line in case B recombination circumstances (Osterbrock 1989). Because the lowest H α line flux detected is $\sim 0.55 \times 10^{-17}$ erg cm $^{-2}$ s $^{-1}$, candidate Ly α emitters should have a Ly α line flux in excess of $\sim 5.5 \times 10^{-17}$ erg cm $^{-2}$ s $^{-1}$ to have a detectable H α counterpart.

Of the 26 candidate Ly α emitters with EW₀ > 15 Å and $\Sigma > 3$ in the area covered by the infrared observations, nine have line fluxes $> 5.0 \times 10^{-17}$ erg cm $^{-2}$ s $^{-1}$. Six of the latter are part of the extended Ly α halo of 1138–262. We will discuss the other three here in more detail. For candidate 561 a line flux of 6.8×10^{-17} erg cm $^{-2}$ s $^{-1}$ was derived from the imaging observations, but spectroscopic observations (described in paper II) indicate a flux of 4.0×10^{-17} erg cm $^{-2}$ s $^{-1}$. For this Ly α flux level, we do not expect to observe H α emission. Candidate 778 has a Ly α line flux of 67.6×10^{-17} erg cm $^{-2}$ s $^{-1}$ (outside the range of fluxes displayed in Fig. 13) and coincides with an object detected on the NB 2.07 image with a H α flux of 8.8×10^{-17} erg cm $^{-2}$ s $^{-1}$, resulting in a Ly α /H α ratio of 7.7.

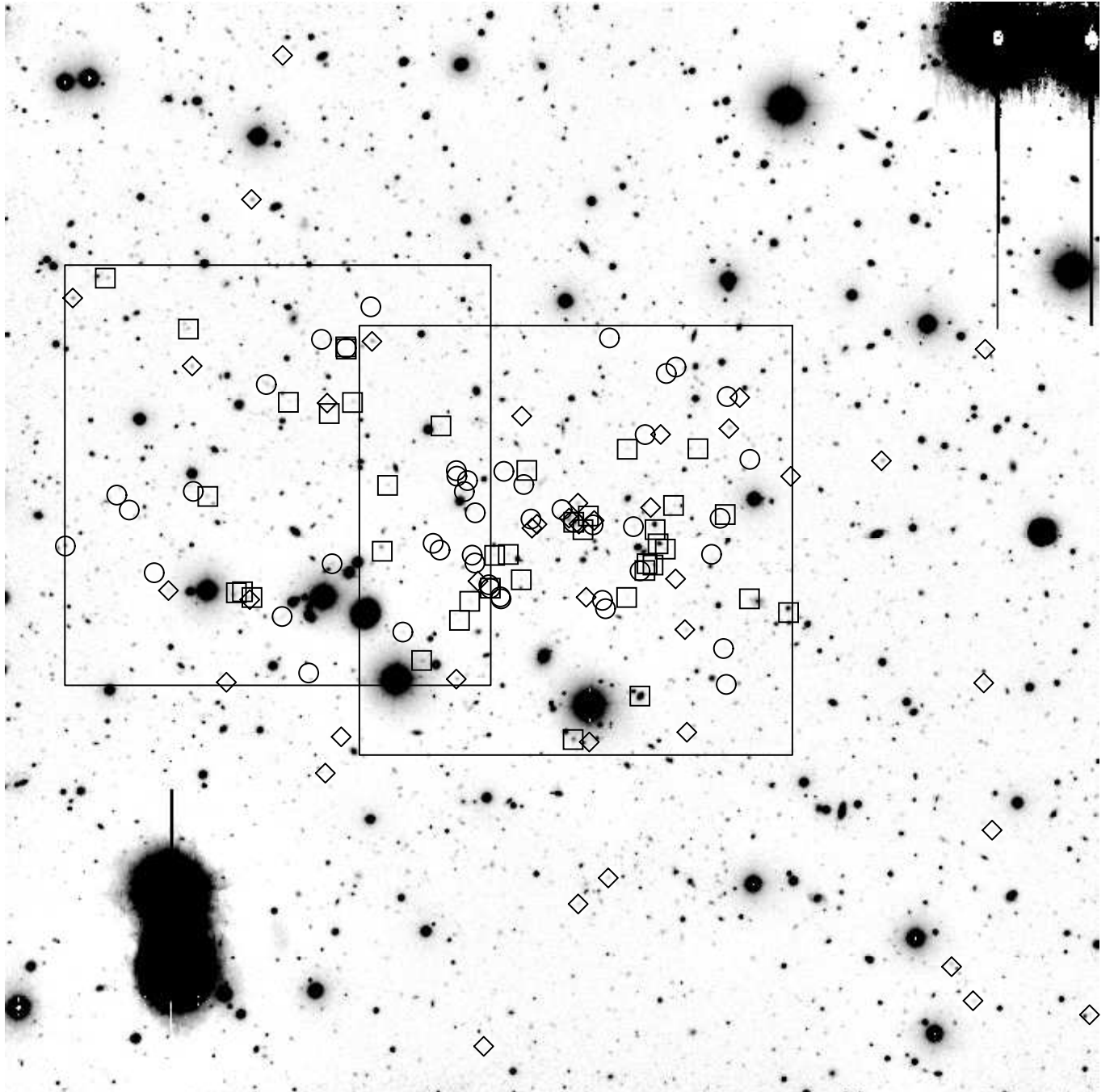


Fig. 12. A 6.8×6.8 I band image of the field of PKS 1138–262. Candidate Ly α emitters are indicated by diamonds, candidate H α emitters by squares and EROs by circles. The two regions observed in NB 2.07 and K_s band are indicated by the boxes.

The object has an H α EW₀ of 18 Å and is therefore not included in the list of candidate H α emitters. The emitter is further described in Sect. 5.4. Candidate 441 is part of a chain of emitters (confirmed in Paper II), emitting both Ly α and H α , having a Ly α /H α ratio of 4.7. The Ly α emitter does not coincide with a candidate H α emitter, because there is no object detected at this exact location on the NB 2.07 band, but H α candidate 145 is part of the same chain and only 1.3'' away.

Only one candidate Ly α emitter with Ly α line flux below 5.5×10^{-17} erg cm $^{-2}$ s $^{-1}$ emits detectable H α : candidate 675 has a Ly α flux of 3.1×10^{-17} erg cm $^{-2}$ s $^{-1}$ and an H α flux of 0.7×10^{-17} erg cm $^{-2}$ s $^{-1}$, resulting in a ratio of 4.4 (see Fig. 13). The object was not selected as an H α candidate emitter as its significance (Σ) is only 1.7. The lower limits of the Ly α /H α ratio computed for the remaining objects (see Fig. 13) are in the range 2–7.

For 31 of the 40 candidate H α emitters with EW₀ > 25 Å and $\Sigma > 2$ we detect no Ly α emission. The up-

per limits for the Ly α /H α ratio for these objects are in the range 0.03 – 1.06. Excluding three objects in the halo of 1138–262, there are six H α candidates for which Ly α emission is detected. Their ratios are in the range 0.10 – 0.73 (see Fig. 13).

Note that the H α and Ly α emission for respectively the candidate Ly α and H α emitters has been measured in the apertures defined on respectively the NB 0.38 and NB 2.07 images. This can cause differences in the Ly α /H α ratios for these objects within a factor two. This discrepancy is, however, not large enough to explain the obvious difference in ratios between the two types of candidates: candidate Ly α emitters have Ly α /H α ratios > 2 , while candidate H α emitters have ratio < 1 . It is easily understood that objects selected by Ly α emission must have dust free sightlines and therefore Ly α /H α ratios close to the case B value. There is no **such** selection bias towards low Ly α /H α ratios for objects selected by H α emission, but as star formation is generally accompanied by dust production, it is not surprising that the candidate H α emitters have low Ly α /H α ratios.

The spatial positions of the candidates for which both Ly α and H α has been detected are indicated on Fig. 7 and Fig. 10.

5.2. Star formation rates

5.2.1. SFR estimators

If clouds of neutral hydrogen in or near high redshift galaxies absorb the integrated stellar light shortward of the Lyman limit and re-emit this energy in nebular lines, such as Ly α and H α , they provide a direct, sensitive probe of the young massive stellar population. Since only stars with lifetimes shorter than 20 Myr contribute significantly to the integrated ionizing flux of the galaxy, emission line flux is a nearly instantaneous measure of the star formation rate (SFR). This emission line flux can be computed by stellar population synthesis models, but is very sensitive to the initial mass function (IMF) assumed since almost exclusively stars with $M > 10 M_{\odot}$ contribute (Kennicutt 1998). Assuming a Salpeter (1955) IMF with mass limits 0.1 and 100 M_{\odot} and solar metallicity, Kennicutt derives, using the evolutionary synthesis models of Kennicutt et al. (1994), the following relation:

$$\text{SFR (M}_{\odot}\text{yr}^{-1}) = 7.9 \times 10^{-42} L_{\text{H}\alpha} (\text{erg s}^{-1}) \quad (2)$$

Another way to measure the SFR is observing directly the rest frame ultra violet light, which is dominated by young stars. The optimal wavelength range is 1250 to 2500 Å, longward of the Ly α forest but short enough that older stellar populations do not contribute significantly. Using the same stellar population as described above, for a model galaxy with continuous star formation during ~ 100 Myr, Kennicutt (1998) finds that the luminosity in this wavelength region scales directly with the SFR:

$$\text{SFR (M}_{\odot}\text{yr}^{-1}) = 1.4 \times 10^{-28} L_{\nu} (\text{erg s}^{-1}\text{Hz}^{-1}) \quad (3)$$

This conversion is, however, dependent on the age of the stellar population and mode of star formation. The SFR / L_{ν} ratio is higher⁴ in populations younger than 100 Myr, up to 57% for a 9 Myr old population and lower in 100 Myr old populations with, for example, an exponentially decreasing star formation rate. Glazebrook et al. (1999) extensively discuss the dependence of luminosity of the H α line, 1500Å and 2800Å continuum on age and metallicity of the galaxy stellar population.

5.2.2. SFRs of candidate H α emitters

We have computed the $\text{SFR}_{\text{H}\alpha}$ from the H α emission of the candidate H α emitters assuming they are at $z = 2.16$, correcting for a 25% contribution of the [N II]6548+6584 Å system (Kennicutt & Kent 1983). For the IMF used to compute Eq. 3, the UV spectrum happens to be nearly flat in L_{ν} (Kennicutt 1998). The central wavelength of our I band observations corresponds to 2430 Å in the rest frame of objects at $z = 2.16$ and is therefore suitable to estimate the SFR_{uv} of galaxies in the proto-cluster. Because we do not correct for possible absorption by dust, both star formation estimators can be considered lower limits to the intrinsic star formation in the galaxies.

Excluding the radio galaxy components, a QSO (see Sect. 5.4) and a low-redshift interloper (see Table A.1), the SFRs derived from the H α (UV) emission are in the range 2 – 32 (3 – 52) M_{\odot} yr $^{-1}$. The ratio of $\text{SFR}_{\text{H}\alpha}$ / SFR_{uv} is in the range 0.3 – 2.5 with a mean of 0.8 ± 0.1 and a dispersion of 0.5 (see Fig. 14).

Recently, Buat et al. (2002) have investigated the star formation rate determined by the H α line and the UV flux in a sample of nearby star forming galaxies in clusters. They find a mean ratio $\text{SFR}_{\text{H}\alpha}$ / SFR_{uv} of 0.8 ± 0.4 and conclude that within the error bars the two SFR estimators give consistent results. There is however a large scatter in the sample, with two galaxies which exhibit an observed ratio of ~ 0.15 . The mean ratio for an accompanying sample of 19 starburst galaxies is ~ 2 , indicating that more dust is present in these objects. These results were obtained with conversion factors for luminosity to SFR significantly different from Kennicutt's values due to a higher low mass cutoff of the IMF and the use of another population synthesis program (Starburst99, Leitherer et al. 1999), but the ratio of SFR values is (coincidentally) exactly equal and their results are therefore comparable with ours. Assuming different IMFs, low and high mass cutoffs and periods since the burst for model stellar populations, they obtain a theoretical range of ratios of 0.66 to 1.5 for dust free galaxies. Note that, although the methods give identical values for the ratios, we would obtain values 50% higher using the equations in Sect. 4.1 of Buat et al. (2002) due to the I band sampling 2430 Å in stead of 2000 Å.

⁴ There is an error in Sect. 2.2 of Kennicutt (1998): the SFR/ L_{ν} ratio will be significantly *higher* in younger populations (Kennicutt, private communication).

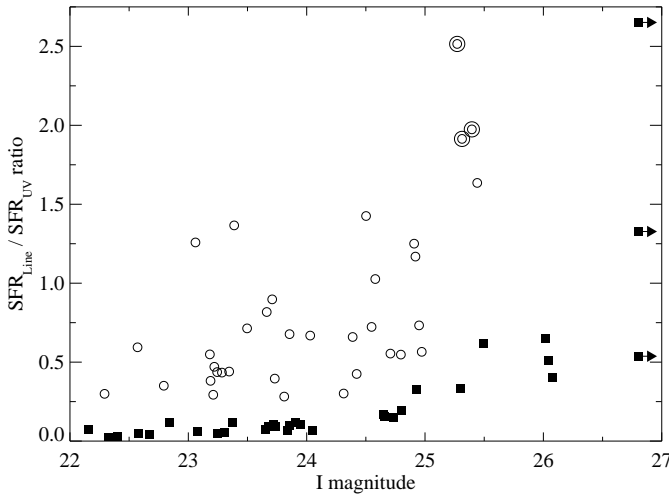


Fig. 14. The ratio of SFR derived from line emission to SFR derived from the rest frame UV continuum emission versus I magnitude for candidate $\text{H}\alpha$ emitters (open circles) and candidate $\text{Ly}\alpha$ emitters (filled boxes). Large circles indicate emitters coinciding with EROs. The three $\text{Ly}\alpha$ emitters plotted at $I = 26.8$ are not detected in the I band. Components of 1138–262, two known QSOs and one low redshift interloper are excluded from the plot.

The ratios of $\text{SFR}_{\text{H}\alpha} / \text{SFR}_{\text{uv}}$ for our sample are consistent with the values determined by Buat et al. (2002). Ratios > 1 can be explained by the presence of dust in the galaxies which extinguishes the UV continuum more effectively than the $\text{H}\alpha$ emission. The three candidate $\text{H}\alpha$ emitters which overlap with two EROs are probably the most dusty objects in our sample (see Fig. 14). The relatively strong UV emission of the $\text{H}\alpha$ candidates with ratios < 1 can indicate that the stellar population is older than 30 Myr, when the $\text{H}\alpha$ flux drops steeply, but UV flux persists up to 1 Gyr (Glazebrook et al. 1999). Alternatively, these ratios could be caused by an unconventional initial mass function or a contribution from direct or scattered AGN light to the UV emission. It is also possible that the youngest stars which are responsible for the $\text{H}\alpha$ emission are more enshrouded in dust than the stars responsible for the bulk of the UV emission (Moorwood et al. 2000).

5.2.3. SFRs of candidate $\text{Ly}\alpha$ emitters

Assuming that the $\text{Ly}\alpha$ emission we observe is produced in case B recombination circumstances and not extinguished by dust (as indicated by the $\text{Ly}\alpha/\text{H}\alpha$ ratios and lower limits computed in Sect. 5.1), the strength of the $\text{H}\alpha$ emission of the $\text{Ly}\alpha$ emitters is one tenth that of the $\text{Ly}\alpha$ emission. We use Eq. 2 to derive the SFR from line emission and Eq. 3 from UV emission for the candidate $\text{Ly}\alpha$ emitters. Excluding the radio galaxy, the QSO discovered in Paper II and the QSO described in Sect. 5.4, the range of $\text{SFR}_{\text{Ly}\alpha}$ is $0.4–4.3 \text{ M}_\odot \text{ yr}^{-1}$, while the range of SFR ratios is $0.02–2.65$ with a mean of 0.3 ± 0.1 and a dispersion 0.5 (see Fig. 14). There are only two emitters with a ratio > 1 .

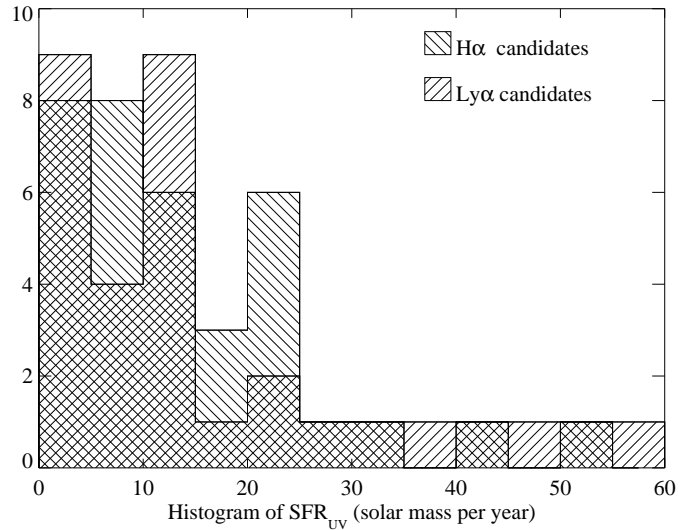


Fig. 15. A histogram of SFR_{uv} for both $\text{H}\alpha$ and $\text{Ly}\alpha$ candidates. The horizontal axis shows the SFR in $\text{M}_\odot \text{ yr}^{-1}$. The bin size is set to $5 \text{ M}_\odot \text{ yr}^{-1}$. The radio galaxy, two QSOs and a low redshift interloper are excluded from this plot.

These are both not detected in the I band. In general, the $\text{SFR}_{\text{Ly}\alpha} / \text{SFR}_{\text{uv}}$ ratios of the $\text{Ly}\alpha$ candidates are much lower than those of the $\text{H}\alpha$ candidates. This might be due to the resonant nature of the $\text{Ly}\alpha$ recombination line. Although we expect the $\text{Ly}\alpha$ candidates to contain almost no dust, $\text{Ly}\alpha$ photons are absorbed and reemitted many times by neutral hydrogen before they escape the galaxies, increasing the chance to be absorbed by dust enormously. In addition, the wavelength of $\text{Ly}\alpha$ is more than 1000 \AA lower than the restframe wavelength of 2430 \AA which the I band samples and suffers therefore more from extinction. The derived values of $\text{SFR}_{\text{Ly}\alpha}$ can therefore be considered as lower limits to the SFRs of the candidates.

5.2.4. SFRs derived from UV emission

To assess whether the samples of $\text{Ly}\alpha$ and $\text{H}\alpha$ candidates have different SFRs, we consider the SFR_{uv} for both kind of emitters (Fig. 15), excluding components of the radio galaxy, the two QSOs (see Sect. 5.4) and one low redshift interloper among the $\text{H}\alpha$ sample. To compute statistical properties of these samples properly taking into account the non-detection, we have employed survival statistics, using the methods presented in the ASURV (1.1) package (Isobe & Feigelson 1990; Lavallee et al. 1992). The range of inferred SFR_{uv} of the $\text{Ly}\alpha$ and $\text{H}\alpha$ sample is $0.8–59 \text{ M}_\odot \text{ yr}^{-1}$ with a mean of $16 \pm 3 \text{ M}_\odot \text{ yr}^{-1}$ and $2.9–52 \text{ M}_\odot \text{ yr}^{-1}$ with a mean of $14 \pm 2 \text{ M}_\odot \text{ yr}^{-1}$, respectively. The distribution of SFRs derived from the I band flux is therefore quite comparable for the two populations. In addition, a Peto-Prentice generalized Wilcoxon test (Prentice & Marek 1979) shows that there is a 62% prob-

ability that the two samples have the same underlying distribution.

Integrating the SFRs of the Ly α and H α emitters, we obtain values of 507 and 501 $M_{\odot} \text{ yr}^{-1}$, respectively. The comoving volumes in which we have found these emitters are 9696 Mpc^3 ($2.110 < z < 2.163$, 43.6 arcmin^2) and 2076 Mpc^3 ($2.114 < z < 2.194$, 12.5 arcmin^2), resulting in SFR densities (SFRDs) of 0.052 and $0.24 M_{\odot} \text{ yr}^{-1} \text{ Mpc}^{-3}$, respectively. Converted to an Einstein-De Sitter cosmology with $H_0 = 50 \text{ km s}^{-1} \text{ Mpc}^{-1}$ (to compare with Madau et al. 1996), the SFRDs of Ly α and H α emitters are 0.070 and $0.32 M_{\odot} \text{ yr}^{-1} \text{ Mpc}^{-3}$, respectively, a factor 4 to 18 more than the fiducial SFRD, as estimated by the mass density of metals observed today divided by the present age of the Universe, which is close to the lower limit of the SFRD at $z \sim 2.75$ (Madau et al.). The observed SFRDs are about a factor ten lower than the SFRD of the nearby Coma and Abell 1367 clusters, as derived from the H α luminosities of selected galaxies in these clusters (Iglesias-Páramo et al. 2002). Note however, that the derived H α luminosities of all our 35 H α candidates are in excess of $10^{41.5} \text{ erg s}^{-1}$, somewhat above the value of L^* found for Coma ($10^{41.23} \text{ erg s}^{-1}$, Iglesias-Páramo et al. 2002). If the Coma cluster were placed at $z = 2.16$, we would not have detected more than one of its members by its H α emission.

Another measure of the star formation activity is the ratio of SFR in a galaxy to its mass. This ratio does not depend on the density of galaxies in the (proto-) cluster. We derive the stellar mass of the candidate H α emitters at $z = 2.16$ from their K band magnitudes as described in Sect. 5.3. The ratio of star formation rate to mass is therefore given by the EW_0 : $\text{SFR} / M \text{ (yr}^{-1}) = 7 \times 10^{-12} \text{ EW}_0 \text{ (\AA)}$. Although the Sloan r' filter used by Iglesias-Páramo et al. (2002) samples a lower restframe wavelength range ($5440\text{\AA} - 6755\text{\AA}$) than our K_s filter ($6408\text{\AA} - 7263\text{\AA}$), we assume here that the flat SED of galaxies above the Balmer break justifies the use of the same formula for the Coma cluster galaxies. There is no bias for EW_0 in the Coma cluster sample, because all Coma galaxies with known velocities (up to $r' \approx 16.5$) are selected. In our sample of H α candidates, we have only selected those with $\text{EW}_0 > 25\text{\AA}$, so we have to exclude the Coma cluster galaxies with $\text{EW}_0 < 25\text{\AA}$. Twelve Coma galaxies remain in the sample, which has a mean EW_0 of 76\AA , while the mean EW_0 of the non-AGN H α candidates is 188\AA . This difference indicates that the star formation rate per unit mass in the proto-cluster galaxies is on average 2.5 times higher than in the Coma cluster galaxies.

5.3. Galaxy masses

Stellar masses for the galaxies are best estimated from infrared magnitudes since at that wavelength range the influence of rare short-lived high mass stars is minimal. The central wavelength of the observed K_s band magni-

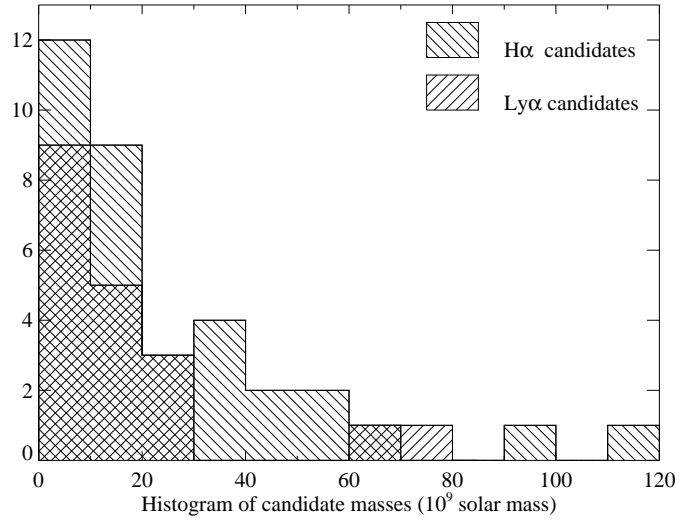


Fig. 16. A histogram of the K_s derived masses for both H α and Ly α candidates. The horizontal axis shows the mass in $10^9 M_{\odot}$. The bin size is $10 \times 10^9 M_{\odot}$.

tudes correspond to 6840 \AA in the rest frame of the galaxies at $z = 2.16$. Since this wavelength is redward of the 4000 \AA break, it is suitable to estimate galaxy masses although maybe not optimal. We have computed an L/M ratio for galaxies at $z = 2.16$ observed through this band using four models of GISSEL93 (Bruzual & Charlot 1993) representing stellar populations with a constant SFR, an exponential SFR and a 10 and 100 Myr burst. The IMF used in these models is a Salpeter (1955) law with lower mass cutoff at $0.1 M_{\odot}$ and upper mass cutoff at $125 M_{\odot}$. Assuming an age of 0.5 Gyr ($z_f = 2.55$) for the stellar populations of the candidate emitters, we obtain M/L ratios in the range of $2.5 - 7.2 M_{\odot} / L_{\odot}$ per L_{\odot} . We will use an M/L ratio of $4.8 M_{\odot} / L_{\odot}$, which is the mean ratio of the four models. At 0.25 Gyr and 0.75 Gyr the mean ratios are respectively 3.3 and $5.7 M_{\odot} / L_{\odot}$. Note that the computed mass to light ratio of ~ 5 in solar units is higher than commonly used ratios at high redshift, because we do not use the bolometric luminosity of the galaxies but only the luminosity in the restframe wavelength range sampled by the K_s band.

Within the area covered by the K_s band images, there are 19 non-AGN Ly α candidates. Four of these (21%) are not detected in K_s band. Of the 35 non-AGN H α candidates, also 4 (11%) are not detected in K_s band. Taking into account the non-detections, the mean flux densities expressed in K magnitude of the Ly α and H α samples are respectively 21.2 ± 0.3 and 20.7 ± 0.2 . We have converted the K magnitudes of the candidates to galaxy masses assuming they are at $z = 2.16$, resulting in a range of masses of $3 - 75$ and $3 - 113 \times 10^9 M_{\odot}$ with means of 17 ± 4 and $26 \pm 4 \times 10^9 M_{\odot}$ respectively. A histogram of masses of the candidate emitters is shown in Fig. 16, which shows that there are only two Ly α emitters with $M > 30 \times 10^9 M_{\odot}$, while there are ten H α emitters in this range. A Peto-Prentice generalized Wilcoxon test

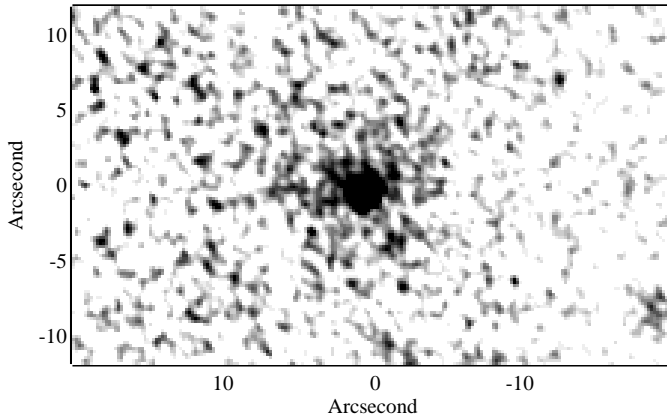


Fig. 17. Morphology of X-ray emitting candidate Ly α emitter 778 accompanied by faint extended Ly α emission. The gray scale represents Ly α line flux (narrow minus broad band), where white is the background level and black is 3 times the rms of the noise in the image. Coordinates of the central position are $\alpha, \delta_{\text{J}2000} = 11^{\text{h}}41^{\text{m}}28.39, -26^{\circ}27'44.6$.

(Prentice & Marek 1979), however, shows that there is a 20% probability that the two samples have the same underlying distribution. We conclude that there is tentative evidence that the candidate H α emitters are more massive than the candidate Ly α emitters.

The total mass of the non-AGN Ly α and H α emitters derived from the detected K band magnitudes is respectively 3.1 and $8.9 \times 10^{11} \text{ M}_\odot$.

5.4. X-ray properties

The properties of X-ray point sources in the field of PKS 1138–262 are presented in a separate paper (Pentericci et al. 2002). Here, we only mention that three X-ray point sources exhibit Ly α emission and one H α emission. One of these does not emit sufficient Ly α emission to be included in our catalogue ($\text{EW}_0 = 3.2 \text{ \AA}$, $\Sigma = 3.6$). A second (Ly α candidate 968) is indeed spectroscopically confirmed to be a QSO (see Paper II). A third (Ly α candidate 778) has a very high equivalent width ($\text{EW}_0 = 311 \text{ \AA}$). In addition, it displays a faint Ly α halo with a size of about $10''$, visible in the convolved image (Fig. 17). It was not included in the catalogue of Paper I and has not been observed spectroscopically because it is not covered by all jittered NB 0.38 images. The presence of a halo, high EW, high Ly α line flux ($6.7 \times 10^{-16} \text{ erg cm}^{-2} \text{ s}^{-1}$) and X-ray emission are consistent with an AGN nature of this object. The near infrared spectrum of H α candidate 215 emitting X-rays is presented in a forthcoming paper, which confirms the AGN nature of this object.

5.5. Conclusions on galaxy properties

Using imaging observations in six bands, we have investigated several galaxy populations possibly present in a

proto-cluster at $z = 2.16$. From a selection on $I - K_s$ colour, we find several EROs. The colours of these objects are not consistent with the colours computed for evolved ellipticals at $z \sim 2$. However, the number density of EROs is high and is increasing towards the radio galaxy, indicating that some of the red objects must be associated with the radio galaxy structure. The EROs could represent the progenitors of cluster ellipticals with some star formation still going on. The presence of excess emission consistent with H α radiation at $z = 2.16$ from two of the observed EROs supports this idea. A second sample is formed by the objects selected on NB 2.07 – K_s colour. We believe that most of these objects are H α emitting galaxies at $z = 2.16$, associated with the structure of galaxies around the radio galaxy. The increase of the number density of these objects towards the radio galaxy again supports this view. The high EWs of some candidate H α emitters have to be explained by an AGN contribution, but most emitters should be powered by star formation with a rate of $10 - 100 \text{ M}_\odot \text{ yr}^{-1}$. This is also true for the sample of candidate Ly α emitters selected on the basis of NB 0.38 – B colour.

We have compared the properties of the Ly α and H α emitters. The density of H α emitters is higher close to PKS 1138–262, their Ly α /H α ratios are lower than for the Ly α emitters and their K_s band emission and implied masses are higher on average. We propose the following scenario to explain the observed differences. A larger fraction of the Ly α emitters is still being accumulated from the environment as compared with the H α emitters, while the more massive H α emitters have been able to retain more metal rich gas and dust resulting in a lower Ly α /H α ratio.

6. PKS 1138–262: a rich distant cluster?

In this section we investigate the cluster properties of the structure associated with radio galaxy PKS 1138–262.

6.1. The overdensity of Ly α emitters in redshift space

In Paper II, we have presented the redshift distribution of the 15 confirmed Ly α emitters. This distribution (see Fig. 3 in Paper II) does not follow the sensitivity curve of the narrow band filter used to select the candidate Ly α emitters, but is narrower and centered on the redshift of the radio galaxy, indicating that the Ly α emitters have a physical connection to the central radio galaxy. To quantify the significance of this deviation from randomness we have carried out Monte Carlo simulations of the distribution of redshifts observed through the narrow band filter. We have simulated 10,000 realizations of the redshift distribution of 14 Ly α emitters. The redshift of each simulated emitter was chosen according to the probability function derived from the sensitivity of the NB 0.38 filter and the VLT overall efficiency. The mean and standard deviation of each realization is plotted in Fig. 18. The mean ($z = 2.155$) and standard deviation ($\delta z = 0.0109$) of the

redshift distribution of the confirmed Ly α emitters is indicated by a cross on this figure, which diverge respectively 2.0σ and 2.4σ from the simulated values⁵. The measured distribution deviates therefore 3.1σ from a random distribution, meaning that the probability that the redshifts of the confirmed Ly α emitters are drawn from a such a distribution is less than 0.2%. This shows that the ensemble of Ly α emitters must have a physical connection with the central radio galaxy.

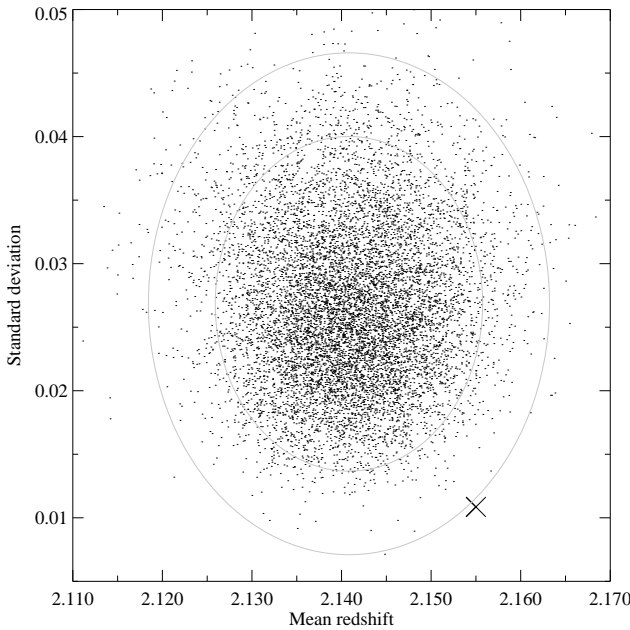


Fig. 18. The mean and standard deviations of the 10,000 simulated redshift distributions. The cross indicates the position of the measured redshift distribution of the confirmed Ly α emitters and the contours indicate the 2 and 3σ deviation from the combined mean and standard deviation from the simulated distributions.

6.2. Mass and overdensity of the proto-cluster

In Paper II the mass of the proto-cluster and volume density of the Ly α emitters was shortly discussed. A more thorough discussion follows here.

We can consider two limiting cases of the dynamical state of the structure of galaxies: it is detached from the Hubble flow and completely virialized or it is no dynamical entity at all and the galaxies move according to the expansion of the Universe. In the first case, the velocities of the galaxies are representative of the potential well of the

⁵ Note that the narrow band filter was designed for the cone angle of FORS1 and its transmission was measured within the instrument. The measured deviation of the mean redshift can therefore not be due to the dependence of interference filter specifications on the incident beam.

cluster, while in the latter case the redshifts are directly related to distances.

In the first case, we can compute a virial mass as an estimate of the cluster mass. The group of galaxies at $z \sim 2.16$ consists of 15 members, including PKS 1138–262 but excluding the QSO at $z = 2.183$, which is a 3σ outlier. The redshift distribution of the members is bimodal around the radio galaxy (see Paper II). The velocities v_i of the galaxies relative to the mean velocity of the group are computed in the following way:

$$v_i = c (z_i - \bar{z}) / (1 + \bar{z}). \quad (4)$$

The velocity dispersion of the two groups of 7 members each (the radio galaxy is excluded in this case) is 385 km s^{-1} and 204 km s^{-1} , as computed by the Gapper sigma method (Beers et al. 1990), which is considerably smaller (23%) than computed by the standard method (square root of variance). The velocity dispersion of the entire sample is 901 km s^{-1} , as computed by the Gapper sigma method, which is 10% smaller than by the standard method.

The virial radius R_v and mass M_v of N cluster members at positions r_i with velocity dispersion σ_v is computed as follows:

$$R_v = \pi \frac{1}{2} \frac{N(N-1)}{2} \left(\sum_{i < j} \frac{1}{|r_i - r_j|} \right)^{-1}, \quad (5)$$

$$M_v = \frac{6}{G} \sigma_v^2 R_v. \quad (6)$$

Small et al. (1998) show that the virial mass estimator works reasonable well even for a bound system with substantial substructure. If the system is only marginally bound, the estimate is too high but not more than a factor of two. The largest uncertainties in our estimate are the unknown dynamical state (i.e. one group or two groups, bound or unbound) and the small number of available redshifts.

The virial radii of the two groups are 0.8 and 1.1 Mpc, about two thirds of the maximum observable radius of 1.5 Mpc which was fixed by the size of the CCD. The virial masses of the groups are therefore 1.7 and $0.6 \times 10^{14} \text{ M}_\odot$. The mass of the two groups together ($2.3 \times 10^{14} \text{ M}_\odot$) is much smaller than the virial mass computed for the group of 14 galaxies as a whole ($14 \times 10^{14} \text{ M}_\odot$).

In the second case, we assume that the emitters just detached from the Hubble flow and are now collapsing to a common center of gravity. In this case the redshifts of the emitters can be used as distance indicators with a small correction for their motion towards each other. We can compute the comoving space density of Ly α emitters, its associated galaxy over-density and from this, derive a mass over-density. To compute the space density, we only consider the 14 confirmed emitters of Paper II in the redshift range $2.139 \leq z \leq 2.170$. The (uncorrected) comoving volume corresponding to this range is 5611 Mpc^3 .

The comoving volume density of the confirmed emitters is therefore 0.0025 Mpc^{-3} , a factor 1.4 smaller than the density found in for the LBG peak at $z = 3.09$ (S00). Because not all candidates were observed and some were too faint to produce a detectable line in their spectra, the resulting over-density of 4.4 ± 1.2 with respect to the field population of Ly α emitters is a lower limit.

The total mass of the structure can be estimated by following Steidel et al. (1998)

$$M = \bar{\rho} V (1 + \delta_m) = 6.6 \times 10^{15} M_\odot (1 + \delta_m) \quad (7)$$

with $\bar{\rho}$ the mean density of the universe and δ_m the mass over-density within the volume containing the confirmed emitters. The mass density is related to the galaxy over-density δ_{gal} through

$$1 + b\delta_m = C (1 + \delta_{\text{gal}}), \quad C = 1 + f - f(1 + \delta_m)^{(1/3)} \quad (8)$$

where b is the bias parameter, C takes into account the redshift space distortions caused by peculiar velocities and f is the velocity factor (Peebles 1993). This factor depends on the redshift and its value is 0.96 for $z = 2.16$. From the statistics of peaks in the redshift distribution of LBGs, Steidel et al. (1998) argue that $b \geq 4$. Taking b in the range 3–5, δ_m is estimated to be 0.6–1.2. This implies a mass of our structure of $(1.1 - 1.5) \times 10^{16} M_\odot$.

The age of the universe at $z = 2.155$ is 3.7 Gyr, while the crossing time for each group is about 3 Gyr. It is therefore impossible for the system around 1138–262 to be in a relaxed state since it takes a few crossings of the cluster members to virialize. Hubble flow expansion of the galaxies could lead to an artificially enlarged *velocity dispersion*. The *virial* mass of $1.4 \times 10^{15} M_\odot$ must therefore be considered an upper limit to the mass of the bound (part of the) system. Similarly, part of the mass computed with the second method is not bound to the system. Following the same procedure for the used volume without an over-density results in a mass of $6.5 \times 10^{15} M_\odot$. This mass is mostly intergalactic gas which will disappear out of the cluster with the Hubble flow. A more conservative estimate of the bound mass at $z = 2.16$ is therefore $4 - 8 \times 10^{15} M_\odot$, although the true bound mass of the system is probably much lower, which does not exclude the possibility that more mass will be bound at a later time.

6.3. Conclusions on cluster properties

Using the lists of clusters members selected in the first part of this paper, we have investigated the cluster properties of the galaxies in the field of PKS 1138–262. About 5% of the galaxies in the local universe are gathered in groups or clusters whose space density is larger than one galaxy per cubic megaparsec, about two orders of magnitude greater than the average density (Dressler 1984). Dense and populous clusters (as defined and cataloged by Abell 1958) contain on the order of 100 galaxies within two orders of magnitudes of the third brightest member. The cluster members are gravitationally bound and to

a large extent in dynamical equilibrium (i.e. virialized). Because the universe is about 4 Gyr old at $z = 2.2$, we do not expect large virialized systems by that time and we will therefore call the over-density of objects around PKS 1138–262 a proto-cluster which will develop into a cluster. The evidence for an over-density of galaxies associated with the radio galaxy comes from the high density of K_s band galaxies and ERO counts as compared with field counts and the indication that most of this over-density is located in a $40''$ region around the radio galaxy. The density of K band sources near the radio galaxy corresponds to the density of current day's clusters richer than class 0 or 1. Furthermore, the density of candidate H α emitters is similar or higher than the density found around other known high redshift (active) galaxies and is clearly highest in the $40''$ region around PKS 1138–262. Finally, the comoving volume density of candidate Ly α emitters in the field of the radio galaxy is higher than in a blank field, if compared to the number of Ly α emitters in the field at $z = 2.4$ and 3.4 (Stiavelli et al. 2001; Cowie & Hu 1998) and in the over-density of LBGs at $z = 3.09$ found by Steidel et al. (2000). From the imaging alone, we conclude that PKS 1138–262 is located in an over-density of galaxies, while the spectroscopical observations provide additional confirmation. The 14 Ly α emitters with redshifts confirmed by spectroscopy have a redshift distribution which shows that they are clearly associated with the radio galaxy. The probability that we have observed a rare realization of randomly distributed emitters is less than 0.4%. The comoving volume density of the confirmed emitters is already higher than in the field and is only a subset of the emitters in the volume. We therefore conclude that PKS 1138–262 is located in a density peak which will most probably evolve into a cluster of galaxies.

An indication that the proto-cluster is not virialized comes from the lack of extended X-ray emission perpendicular to the radio sources axis (Carilli et al. 2002). These observations imply an upper limit to the 2–10 keV luminosity of an extended relaxed cluster atmosphere of $1.5 \times 10^{44} \text{ erg s}^{-1}$, less than 40% of the X-ray luminosity of the Cygnus A cluster. Given the unrelaxed state of the system, it is not possible to make an estimate of the bound mass at $z = 2.16$, but an upper limit of $\sim 10^{15} M_\odot$ is computed for a virialized system with the properties of the PKS 1138–262 proto-cluster.

Finally, we consider the galaxy population in the proto-cluster. As discussed in Sect. 4.2, there is a population of EROs present in the cluster, most plausibly identified with dusty star forming galaxies. Contrary to what is observed in low redshift clusters, we do not observe a sequence due to passive ellipticals in the $J - K$ vs K colour-magnitude diagram, presented in Fig. 19. Both results are consistent with the idea that cluster galaxies have evolved and were more luminous and bluer at high redshift (e.g. van Dokkum et al. 1998).

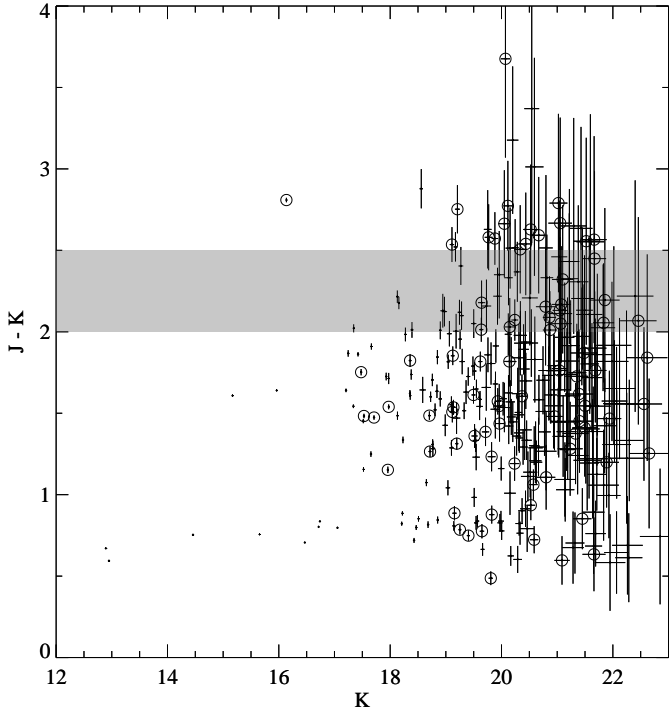


Fig. 19. Colour-magnitude plot of $J - K$ vs K for the 306 bona fide sources detected on the K_s and J band images. The sources within $40''$ of the radio galaxy are indicated by circles and the expected locus of the sequence of passive cluster ellipticals at $z = 2.2$ is indicated by the grey bar. The $J - K$ locus is computed from the model defined in Sect. 4.2.2 (see also Fig. 4).

7. Summary

We have presented new near infrared and optical imaging of the field of radio galaxy PKS 1138–262 at $z = 2.16$. From these data and published optical imaging and spectroscopy, we find several galaxy populations associated with the radio galaxy.

- In the 12.5 square arcminute field covered by the K_s band images, we detect 550 objects in K_s . The number density of K band sources is about 1.5 times higher than blank field counts and increases towards the radio galaxy.

- In the same area, we find 44 objects with $I - K > 4.3$. The surface density of EROs is about a factor two higher than the mean density found in blank fields. Because the density of EROs increases towards the radio galaxy, we conclude that some of the EROs are galaxies at $z \sim 2.2$ and associated with the radio galaxy. Most of these are star forming galaxies reddened by dust, although up to five may be passive ellipticals.

- Also in the same area, we find 40 candidate $H\alpha$ emitters. The density of the brightest emitters is comparable to the density in other AGN fields and, again, increases towards the radio galaxy. The upper limit to the $Ly\alpha/H\alpha$ ratio of these sources is 1.1, but for most candidates the ratio is much smaller, meaning that these objects contain some dust or neutral hydrogen. Two $H\alpha$ candidates are

also identified as EROs. These must be dusty starbursts at $z \sim 2.2$.

- In the effective 43.6 square arcminute area of the optical images, we find 40 candidate $Ly\alpha$ emitters. The surface density of these candidates does not show an increase towards the radio galaxy. The $Ly\alpha/H\alpha$ ratio of the 26 $Ly\alpha$ candidates in the area covered by infrared imaging is in the range 2–7. The sight lines through which we observe the $Ly\alpha$ radiation are therefore relatively dust free.

- The SFRs derived from rest frame UV flux of the sample of $H\alpha$ and $Ly\alpha$ candidates are comparable, but the galaxy masses derived from the flux around $\sim 7000\text{\AA}$ are on average larger for the $H\alpha$ candidates than for the $Ly\alpha$ candidates. From the spatial distribution of the two samples, we deduce that the $H\alpha$ emitters are more settled into the potential well of the proto-cluster than the $Ly\alpha$ emitters.

- From the spatial distribution, number density and redshift distribution of objects detected in the field of PKS 1138–262, we conclude that the radio galaxy is located in a density peak which will evolve into a cluster of galaxies at the present day. The bound mass at $z = 2.16$ is $10^{15} M_\odot$ at most.

The structure around PKS 1138–262 is one of the few proto-clusters known at $z > 2$ and deserves further study. X-ray observations of this field have been carried out by Carilli et al. (2002) and an analysis of the X-ray point sources and AGN content of the proto-cluster is presented in Pentericci et al. (2002). Infrared spectroscopy of a small sample of the candidate $H\alpha$ emitters has been carried out and will be reported in Kurk et al. (in preparation).

Acknowledgements. We acknowledge productive discussions with B. Venemans, M. Jarvis and J. Fynbo. J. Fynbo kindly provided the algorithm for the Monte Carlo simulation of $Ly\alpha$ emitter redshift distributions (Sect. 6.1). We thank the referee for its comments which have improved the paper. This research has made use of the NASA/IPAC Extragalactic Database (NED) which is operated by the Jet Propulsion Laboratory, California Institute of Technology, under contract with the National Aeronautics and Space Administration. We have also made use of NASA's Astrophysics Data System Bibliographic Services.

References

- Abell, G. O. 1958, ApJS, 3, 211
- Bahcall, N. A. 1981, ApJ, 247, 787
- Bahcall, N. A. & Fan, X. 1998, ApJ, 504, 1
- Beers, T. C., Flynn, K., & Gebhardt, K. 1990, AJ, 100, 32
- Bertin, E. & Arnouts, S. 1996, A&AS, 117, 393
- Best, P. 2000, MNRAS, 317, 720
- Bower, R. G., Lucey, J. R., & Ellis, R. S. 1992, MNRAS, 254, 601
- Bruzual, A. G. & Charlot, S. 1993, ApJ, 405, 538
- Buat, V., Boselli, A., Gavazzi, G., & Bonfanti, C. 2002, A&A, 383, 801

Bunker, A., Warren, S., Hewett, P., & Clements, D. 1995, MNRAS, 273, 513

Butcher, H. & Oemler, A. 1984, ApJ, 285, 426

Carilli, C., Harris, D., Pentericci, L., et al. 2002, ApJ, 567, 781

Carilli, C. L., Röttgering, H. J. A., van Ojik, R., Miley, G. K., & van Breugel, W. J. M. 1997, ApJS, 109, 1

Cowie, L. L. & Hu, E. M. 1998, AJ, 115, 1319

Cowie, L. L., Songaila, A., Hu, E. M., & Cohen, J. G. 1996, AJ, 112, 839

Daddi, E., Cimatti, A., Pozzetti, L., et al. 2000, A&A, 361, 535

Daddi, E., Cimatti, A., & Renzini, A. 2000, A&A, 362, L45

De Breuck, C., van Breugel, W., Röttgering, H. J. A., & Miley, G. 2000, A&AS, 143, 303

De Breuck, C., van Breugel, W., Stanford, S. A., et al. 2002, AJ, 123, 637

De Propris, R., Stanford, S. A., Eisenhardt, P. R., Dickinson, M., & Elston, R. 1999, AJ, 118, 719

Dey, A., Graham, J. R., Ivison, R. J., et al. 1999, ApJ, 519, 610

Donahue, M., Voit, G. M., Gioia, I., et al. 1998, ApJ, 502, 550

Dressler, A. 1984, ARA&A, 22, 185

Eggen, O. J., Lynden-Bell, D., & Sandage, A. R. 1962, ApJ, 136, 748

Eke, V. R., Cole, S., & Frenk, C. S. 1996, MNRAS, 282, 263

Elston, R., Rieke, G. H., & Rieke, M. J. 1988, ApJ, 331, L77

Elston, R., Rieke, M. J., & Rieke, G. H. 1989, ApJ, 341, 80

Feigelson, E. D. & Nelson, P. I. 1985, ApJ, 293, 192

Fynbo, J. U., Møller, P., & Thomsen, B. 2001, A&A, 374, 443

Fynbo, J. U., Møller, P., Thomsen, B., et al. 2002, A&A, 388, 425

Fynbo, J. U., Thomsen, B., & Møller, P. 2000, A&A, 353, 457

Gladders, M. D. & Yee, H. K. C. 2000, AJ, 120, 2148

Glazebrook, K., Blake, C., Economou, F., Lilly, S., & Colless, M. 1999, MNRAS, 306, 843

Hamuy, M., Suntzeff, N. B., Heathcote, S. R., et al. 1994, PASP, 106, 566

Hamuy, M., Walker, A. R., Suntzeff, N. B., et al. 1992, PASP, 104, 533

Hill, G. J. & Lilly, S. J. 1991, ApJ, 367, 1

Hoeg, E., Bässgen, G., Bastian, U., et al. 1997, A&A, 323, L57

Hu, E. M., Cowie, L. L., & McMahon, R. G. 1998, ApJ, 502, L99

Iglesias-Páramo, J., Boselli, A., Cortese, L., Vilchez, J. M., & Gavazzi, G. 2002, A&A, 384, 383

Infante, L. 1987, A&A, 183, 177

Isobe, T. & Feigelson, E. 1990, in Bulletin of American Astronomical Society, Vol. 22, 917

Ivison, R. J., Dunlop, J. S., Smail, I., et al. 2000, ApJ, 542, 27

Jarvis, M. J., Rawlings, S., Eales, S., et al. 2001, MNRAS, 326, 1585

Kauffmann, G. 1996, MNRAS, 281, 487

Kauffmann, G. & Charlot, S. 1998, MNRAS, 294, 705

Kennicutt, R. 1998, ARA&A, 36, 189

Kennicutt, R. & Kent, S. 1983, AJ, 88, 1094

Kennicutt, R. C., Tamblyn, P., & Congdon, C. E. 1994, ApJ, 435, 22

Kron, R. G. 1980, ApJS, 43, 305

Kurk, J., Röttgering, H., Pentericci, L., et al. 2000a, A&A, 358, L1

Kurk, J. D., Röttgering, H. J. A., Pentericci, L., & Miley, G. K. 2000b, in Conference Series of Revista Mexicana de Astronomía y Astrofísica, Vol. 13, Emission Lines from Jet Flows, Isla Mujeres, November 13-17, 2000, ed. W. Henney, W. Steffen, L. Binette, & A. Raga, 21

Lacy, M., Laurent-Muehleisen, S. A., Ridgway, S. E., Becker, R. H., & White, R. L. 2001, ApJ, 551, L17

Lacy, M., Miley, G., Rawlings, S., et al. 1994, MNRAS, 271, 504

Lavalley, M., Isobe, T., & Feigelson, E. 1992, in Astronomical Data Analysis Software and Systems I, A.S.P. Conference Series, ed. D. M. Worrall, C. Biemesderfer, & J. Barnes, Vol. 1, 245

Leitherer, C., Schaerer, D., Goldader, J. D., et al. 1999, ApJS, 123, 3

Madau, P., Ferguson, H. C., Dickinson, M. E., et al. 1996, MNRAS, 283, 1388

McLure, R. J. & Dunlop, J. S. 2002, MNRAS, 331, 795

Møller, P. & Fynbo, J. U. 2001, A&A, 372, L57

Monet, D., A., B., Canzian, B., et al. 1998, The USNO-A2.0 Catalogue (U.S. Naval Observatory, Washington DC)

Moorwood, A., van der Werf, P., Cuby, J., & Oliva, E. 2000, A&A, 362, 9

Nakata, F., Kajisawa, M., Yamada, T., et al. 2001, PASJ, 53, 1139

Oke, J. 1990, AJ, 99, 1621

Osterbrock, D. E. 1989, Astrophysics of Gaseous Nebulae and Active Galactic Nuclei (University Science Books, Mill Valley CA, USA)

Ouchi, M., Shimasaku, K., Furusawa, H., et al. 2002, ApJ submitted, astro-ph/0202204

Peebles, P. J. E. 1980, The Large Scale Structure of the Universe (Princeton University Press, NJ)

Peebles, P. J. E. 1993, Principles of physical cosmology (Princeton University Press, NJ)

Pentericci, L., Kurk, J., Röttgering, H., et al. 2000a, A&A, 361, L25

Pentericci, L., Kurk, J. D., Carilli, C. L., et al. 2002, A&A, 396, 109

Pentericci, L., Röttgering, H., Miley, G., Carilli, C., & McCarthy, P. 1997, A&A, 326, 580

Pentericci, L., Röttgering, H., Miley, G., et al. 1998, ApJ, 504, 139

Pentericci, L., Van Reeven, W., Carilli, C. L., Röttgering, H. J. A., & Miley, G. K. 2000b, A&AS, 145, 121

Pozzetti, L. & Mannucci, F. 2000, MNRAS, 317, L17

Prentice, R. & Marek, P. 1979, Biometrics, 35, 861

Refregier, A., Valtchanov, I., & Pierre, M. 2002, A&A, 390, 1

Rhoads, J. E. & Malhotra, S. 2001, ApJ, 563, L5

Rhoads, J. E., Malhotra, S., Dey, A., et al. 2000, ApJ, 545, L85

Rosati, P., della Ceca, R., Norman, C., & Giacconi, R. 1998, ApJ, 492, L21

Rosati, P., Stanford, S. A., Eisenhardt, P. R., et al. 1999, AJ, 118, 76

Röttgering, H. J. A., Lacy, M., Miley, G. K., Chambers, K. C., & Saunders, R. 1994, A&AS, 108, 79

Salpeter, E. E. 1955, ApJ, 121, 161

Schlegel, D. J., Finkbeiner, D. P., & Davis, M. 1998, ApJ, 500, 525

Scoggio, M. & Silva, D. 2000, A&A, 359, 953

Small, T. A., Ma, C., Sargent, W. L. W., & Hamilton, D. 1998, ApJ, 492, 45

Stanford, S. A., Eisenhardt, P. R., & Dickinson, M. 1998, ApJ, 492, 461

Stanford, S. A., Elston, R., Eisenhardt, P. R., et al. 1997, AJ, 114, 2232

Stanford, S. A., Holden, B., Rosati, P., et al. 2002, AJ, 123, 619

Steidel, C. C., Adelberger, K. L., Dickinson, M., et al. 1998, ApJ, 492, 428

Steidel, C. C., Adelberger, K. L., Shapley, A. E., et al. 2000, ApJ, 532, 170

Stiavelli, M., Scarlata, C., Panagia, N., et al. 2001, ApJ, 561, L37

Taylor, G. B., Barton, E. J., & Ge, J. 1994, AJ, 107, 1942

van Breugel, W., De Breuck, C., Stanford, S. A., et al. 1999, ApJ, 518, L61

van der Werf, P., Moorwood, A., & Bremer, M. 2000, A&A, 362, 509

van Dokkum, P. G. & Franx, M. 2001, ApJ, 553, 90

van Dokkum, P. G., Franx, M., Kelson, D. D., & Illingworth, G. D. 1998, ApJ, 504, L17

van Dokkum, P. G., Stanford, S. A., Holden, B. P., et al. 2001, ApJ, 552, L101

Venemans, B. P., Kurk, J. D., Miley, G. K., et al. 2002, ApJ, 569, L11

Yan, H., Windhorst, R. A., Odewahn, S. C., et al. 2002, ApJ accepted

Yates, M. G., Miller, L., & Peacock, J. A. 1989, MNRAS, 240, 129

Table A.1. Candidate H α emitters with $EW_0 > 25$ Å and $\Sigma > 2$

ID (1)	Coordinates (2)	<i>K</i> (3)	EW_0 (4)	Σ (5)	$F_{H\alpha}$ (6)
5	11 40 48.4 -26 30 30.6	20.3	89.6	4.4	6.5
^a 29	11 40 46.5 -26 30 14.1	17.7	25.4	15.9	21.3
79	11 40 52.6 -26 30 01.0	20.9	120.2	5.2	4.8
117	11 40 51.6 -26 29 45.9	21.3	73.5	3.0	2.1
131	11 40 51.3 -26 29 38.7	19.3	56.5	9.5	10.9
132	11 40 42.4 -26 29 42.6	19.9	45.8	4.2	5.1
144	11 40 43.5 -26 29 37.4	21.5	246.5	6.2	5.1
145	11 40 57.4 -26 29 37.5	20.3	60.9	3.4	4.4
152	11 40 46.9 -26 29 37.1	23.0	577.2	4.1	2.3
154	11 40 50.7 -26 29 33.7	20.3	47.0	3.4	3.5
155	11 40 57.8 -26 29 35.7	20.1	30.1	2.1	2.7
158	11 40 57.6 -26 29 35.4	21.1	56.9	2.3	2.0
167	11 40 49.8 -26 29 30.5	23.0	278.4	2.2	1.4
176	11 40 46.4 -26 29 26.9	20.1	43.4	3.0	4.0
183	11 40 46.2 -26 29 24.9	20.4	165.0	12.9	10.0
192	11 40 46.3 -26 29 24.4	19.7	26.9	3.2	3.6
^b 199	11 40 48.4 -26 29 08.9	16.1	63.9	110.2	221.9
207	11 40 50.2 -26 29 21.0	21.0	95.1	3.0	3.5
210	11 40 50.6 -26 29 21.4	22.6	139.5	2.4	1.2
211	11 40 53.7 -26 29 20.0	22.0	64.1	2.0	1.0
212	11 40 45.8 -26 29 18.9	21.7	155.2	3.6	2.9
^c 215	11 40 46.0 -26 29 16.9	18.7	99.9	36.3	31.5
229	11 40 46.1 -26 29 11.5	19.1	61.0	11.2	13.5
^b 269	11 40 48.1 -26 29 11.6	20.5	167.3	6.5	9.5
^b 272	11 40 48.0 -26 29 06.5	19.9	38.1	4.3	4.3
279	11 40 44.1 -26 29 05.8	22.6	263.7	2.8	2.0
284	11 40 45.6 -26 29 02.4	22.4	126.4	2.4	1.3
293	11 40 58.6 -26 28 59.6	21.2	115.8	2.9	3.7
310	11 40 53.6 -26 28 55.2	21.8	84.5	2.0	1.5
318	11 40 49.7 -26 28 49.4	23.0	257.8	2.1	1.3
329	11 40 46.9 -26 28 41.4	23.0	2222.2	4.8	4.1
356	11 40 44.9 -26 28 41.1	22.2	81.0	2.0	1.0
375	11 40 52.1 -26 28 32.8	22.3	233.7	2.7	2.3
380	11 40 55.2 -26 28 28.3	22.9	547.1	3.0	2.5
388	11 40 56.4 -26 28 24.1	21.3	100.0	3.8	2.7
394	11 40 54.6 -26 28 24.1	19.8	32.1	3.3	3.8
431	11 40 54.8 -26 28 04.0	20.9	60.6	2.3	2.5
437	11 40 54.8 -26 28 03.2	21.1	71.2	2.4	2.6
457	11 40 59.2 -26 27 56.6	20.9	137.4	8.4	5.3
477	11 41 01.5 -26 27 37.6	21.0	154.1	3.5	5.3

Notes: (1) Catalog number (2) Right ascension and declination in J2000 coordinates (3) *K* band magnitude (4) Rest frame equivalent width (5) Significance of excess flux (6) Continuum subtracted narrow band flux in 10^{-17} erg cm $^{-2}$ s $^{-1}$. Notes to individual objects: ^a Magnitude and morphology indicate that this object is a low redshift interloper, ^b Inside Ly α halo of PKS 1138–262, ^c QSO (see Sect. 5.4).

Appendix A: Source lists

Table A.2. Candidate Ly α emitters with $EW_0 > 15$ Å and $\Sigma > 3$

ID (1)	Coordinates (2)	B (3)	EW ₀ (4)	Σ (5)	F _{Lyα} (6)
28	11:40:50.8 -26:32:26.0	26.1	97.8	4.3	5.3
46	11:40:33.9 -26:32:13.4	25.5	31.6	3.7	3.4
54	11:40:37.1 -26:32:08.3	24.5	24.2	5.6	7.1
73	11:40:37.8 -26:31:55.5	25.7	34.5	3.6	3.1
127	11:40:48.2 -26:31:32.4	25.5	18.9	3.3	2.2
146	11:40:47.4 -26:31:22.6	25.6	26.0	3.5	2.6
184	11:40:36.6 -26:31:04.1	24.9	22.5	4.4	4.4
238	11:40:55.3 -26:30:43.5	26.5	97.5	3.7	3.4
286	11:40:47.9 -26:30:31.5	27.5	265.0	3.1	2.6
297	11:40:54.9 -26:30:29.8	27.5	497.6	3.8	3.4
301	11:40:45.2 -26:30:27.7	27.4	139.9	4.0	2.0
361	11:40:36.9 -26:30:08.8	25.0	23.6	3.8	4.3
365	11:40:58.1 -26:30:09.4	25.0	21.8	3.5	3.7
366	11:40:51.6 -26:30:08.0	25.0	29.5	4.1	5.0
417	11:40:45.3 -26:29:49.1	24.7	18.9	3.8	4.6
441	11:40:57.4 -26:29:38.3	24.9	83.9	4.9	13.5
465	11:40:48.0 -26:29:37.0	26.8	119.2	3.5	3.2
470	11:40:59.7 -26:29:35.0	25.8	49.9	4.2	3.9
479	11:40:51.0 -26:29:31.1	25.3	25.0	3.3	3.3
484	11:40:45.5 -26:29:30.0	27.5	96.6	3.0	1.4
^a 491	11:40:48.2 -26:29:09.5	21.6	108.4	68.3	341.9
^a 515	11:40:48.5 -26:29:07.3	22.7	48.9	23.9	64.3
522	11:40:49.4 -26:29:09.6	23.7	36.0	8.6	20.0
561	11:40:46.2 -26:29:03.2	27.5	9749.7	7.4	6.8
565	11:40:56.6 -26:26:13.6	25.3	28.2	3.0	3.9
674	11:40:46.0 -26:28:35.7	27.5	269.4	3.4	2.6
675	11:40:55.3 -26:28:24.3	26.8	117.8	3.9	3.1
703	11:40:43.7 -26:28:21.8	26.4	86.7	3.4	3.4
728	11:40:36.9 -26:28:03.3	23.7	20.2	7.1	11.9
739	11:40:57.4 -26:27:07.8	24.4	20.6	4.5	6.3
^b 778	11:41:02.4 -26:27:45.1	24.1	314.2	27.4	67.6
877	11:40:54.0 -26:28:01.1	25.3	31.6	3.4	4.3
891	11:40:59.1 -26:28:10.5	25.0	25.4	4.4	4.7
941	11:40:44.0 -26:28:33.5	25.6	32.0	3.1	3.3
942	11:40:49.8 -26:28:29.0	26.2	55.3	3.3	2.9
^c 968	11:40:39.8 -26:28:45.4	24.2	26.6	8.6	9.8
^a 971	11:40:47.8 -26:29:08.2	25.5	334.6	10.6	19.2
980	11:40:42.3 -26:28:51.3	26.3	113.1	3.7	4.7
1009	11:40:49.5 -26:29:11.1	25.1	57.1	5.9	8.5
1017	11:40:48.3 -26:29:01.7	24.2	68.2	8.7	21.5

Notes: (1) Catalog number (2) Right ascension and declination in J2000 coordinates (3) B band magnitude (4) Rest frame equivalent width (5) Significance of excess flux (6) Continuum subtracted narrow band flux in 10^{-17} erg cm $^{-2}$ s $^{-1}$. Notes to individual objects: ^a Inside Ly α halo of PKS 1138-262, ^b QSO described in Sect. 5.4, ^c QSO discovered in Paper II.

Table A.3. Extremely red objects ($I - K > 4.3$)

ID (1)	Coordinates (2)	K (3)	$I - K$ (4)
53	11 40 44.1 -26 30 09.7	21.3±0.2	4.4±0.3
72	11 40 55.8 -26 30 05.8	20.1±0.1	5.2±0.3
95	11 40 44.2 -26 29 56.2	22.0±0.3	4.8±0.4
111	11 40 53.1 -26 29 50.3	20.1±0.1	4.4±0.1
121	11 40 56.5 -26 29 44.6	19.2±0.1	4.3±0.1
151	11 40 47.5 -26 29 41.3	21.5±0.2	5.2±0.6
161	11 40 50.4 -26 29 37.7	20.9±0.1	4.8±0.2
163	11 40 47.6 -26 29 38.2	21.5±0.2	5.9±1.0
166	11 40 50.4 -26 29 37.0	20.7±0.1	5.2±0.3
171	11 40 50.7 -26 29 33.8	20.3±0.1	4.9±0.2
176	11 40 50.7 -26 29 32.5	20.2±0.1	4.7±0.1
189	11 40 46.5 -26 29 27.1	19.2±0.0	4.9±0.1
197	11 41 00.1 -26 29 28.3	20.7±0.1	7.3±1.3
210	11 40 55.1 -26 29 24.7	19.8±0.1	4.5±0.1
215	11 40 51.1 -26 29 24.3	20.9±0.1	5.6±0.4
226	11 40 44.5 -26 29 20.8	20.2±0.1	5.0±0.1
^a 229	11 40 48.4 -26 29 08.8	16.1±0.0	4.7±0.0
233	11 40 51.2 -26 29 21.4	21.4±0.3	5.0±0.6
240	11 40 52.1 -26 29 19.5	20.9±0.2	4.7±0.3
248	11 40 52.3 -26 29 16.9	21.7±0.3	4.6±0.5
255	11 40 48.7 -26 29 04.1	21.7±0.2	5.8±0.9
256	11 41 00.8 -26 29 04.7	21.0±0.2	5.2±0.4
259	11 40 51.1 -26 29 05.4	21.1±0.2	4.4±0.3
267	11 40 59.0 -26 28 57.6	21.9±0.3	4.3±0.4
270	11 40 44.3 -26 29 07.2	19.2±0.1	5.3±0.1
272	11 40 49.6 -26 29 07.7	20.1±0.1	6.0±0.4
282	11 40 47.8 -26 29 09.8	20.4±0.1	4.6±0.2
284	11 40 46.7 -26 29 10.4	20.1±0.1	4.4±0.1
308	11 41 01.2 -26 28 59.1	22.0±0.3	4.7±0.5
343	11 40 51.6 -26 28 51.7	21.0±0.2	4.6±0.3
344	11 40 49.8 -26 28 54.7	19.9±0.1	5.8±0.2
348	11 40 51.4 -26 28 53.3	20.5±0.1	5.1±0.3
351	11 40 51.7 -26 28 49.6	21.4±0.2	4.8±0.4
359	11 40 50.3 -26 28 49.8	21.0±0.1	5.0±0.3
380	11 40 43.5 -26 28 45.0	21.1±0.2	5.1±0.5
402	11 40 46.4 -26 28 35.8	22.1±0.3	4.3±0.4
442	11 40 44.1 -26 28 21.4	21.2±0.1	5.1±0.3
460	11 40 57.0 -26 28 17.4	18.4±0.1	4.5±0.1
463	11 40 45.5 -26 28 10.4	21.4±0.2	5.1±0.5
472	11 40 45.8 -26 28 12.8	20.8±0.1	4.5±0.2
505	11 40 54.8 -26 28 03.6	20.7±0.1	4.4±0.2
506	11 40 55.4 -26 28 00.4	20.6±0.1	4.4±0.2
509	11 40 47.4 -26 27 59.5	20.2±0.1	4.8±0.1
531	11 40 54.1 -26 27 48.1	21.6±0.2	6.5±1.1

Notes: (1) Catalog number (2) Right ascension and declination in J2000 coordinates (3) K band magnitude and error (4) $I - K$ colour and error. Notes to individual objects: ^a PKS 1138-262.